Modal Solutions-based Approach to Relative Dynamics in the Cislunar Environment

Claudio Vela[1], Roberto Opromolla[2], and Giancarmine Fasano[3]
Department of Industrial Engineering, University of Naples "Federico II", Naples, 80125, Italy

Hanspeter Schaub[4]
Department of Aerospace Engineering Sciences, University of Colorado Boulder, Boulder, CO, 80309, United States of America

The raising interest in the cislunar space as a strategic environment to facilitate the access to the surface of the Moon and as an outpost to begin Solar System exploration has fostered the development of several prospective missions in the Earth-Moon system. In particular, close-proximity operations (such as those involving the relative motion of a spacecraft with respect to a lunar station) require the development of specific tools for trajectory design and path-planning. This paper introduces an original relative motion representation with respect to a periodic chief in the circular restricted three-body problem and an original procedure to design proximity trajectories in the cislunar environment based on fundamental modal solutions decomposition. The relative motion model is first developed in a velocity-based orbiting frame, in which the velocity (i.e., flight-path) direction is one of the axes of the frame. Then, modal decomposition is applied to separate the fundamental modes of motion, showing that the modal coefficients, eigenvectors, and eigenvalues can be employed to characterize the geometry of the relative motion. In this way, the coefficients act as geometrically insightful relative orbital elements for trajectory design and path planning purposes.

I. Introduction

The importance of close-proximity operations (CPOs) in the current space environment has become increasingly evident over the years. In the near-Earth space, methodologies for CPOs are being investigated to deal with the current satellite overpopulation by enabling deorbiting as well as a wide range of on-orbit services [1, 2]. In the cislunar space, a similar trend is manifesting [3-7], also in view of its prospective use as a bridgehead for Moon and Solar System exploration. In this respect, different research activities have investigated the feasibility of CPO missions in cislunar space [8, 9], highlighting the importance of an autonomous guidance, navigation, and control (GNC) system, and discussing solutions to comply with low size, weight, and power consumption requirements [10]. To achieve this purpose, however, a deeper understanding of the dynamics of the cislunar space is needed, as well as dedicated models to describe the relative motion of a chaser spacecraft with respect to a target object, due to the higher complexity compared to the near-Earth environment. In this context, this paper focuses on the development of an original relative motion model and its use in conjunction with a fundamental modal solution decomposition to gain geometrical insight for trajectory design and path planning purposes. The resulting formulation can then be leveraged to define relative

---

[1] Research Fellow, Department of Industrial Engineering.
[2] Assistant Professor, Department of Industrial Engineering.
[3] Associate Professor, Department of Industrial Engineering.
[4] Professor and Department Chair, Schaden Leadership Chair, Ann and H.J. Smead Department of Aerospace Engineering Sciences, Colorado Center for Astrodynamics Research. AAS Fellow, AIAA Fellow.

trajectories with desired properties and be used for path-planning purposes, being the coefficients integrals of motions and therefore interpretable as relative orbital elements (ROEs). Thus, the proposed methodology can serve as a key tool within an autonomous guidance sub-system enabling CPOs in the cislunar space.

Relative motion models are often derived within the absolute motion description given in the circular restricted three-body problem (CR3BP), based on two fundamental assumptions: (*i*) circularization, i.e., the two primary centers of gravity, e.g., the Earth and the Moon, revolve in a circular motion; (*ii*) restriction, i.e., the mass of the third body (the spacecraft) is negligible. Within the system of the two primary bodies, the CR3BP formulation allows defining five equilibrium points known as Lagrange points and labelled L1 to L5 around which the motion can be described analytically. For instance, Segerman et al. [11] derive equations and corresponding analytical solutions for the relative motion dynamics of a chaser spacecraft with respect to a target spacecraft in orbit around the L2 point of the Earth/Moon Sun system. Luquette and Sanner [12] derive a set of relative motion dynamics equations for spacecraft orbiting Lagrange points of the Earth/Moon-Sun system under both the CR3BP assumptions and the more general case obtained by removing circularization. However, some GNC applications require high-accuracy modelling of the relative motion: Colagrossi et al. [13] show that, in the Earth-Moon system, this can be achieved only if solar radiation pressure and Sun gravitational effects are considered, as they affect the periodicity of the target orbit. Therefore, they develop a model for guidance and control purposes in an inertial reference frame that can contain such contributions, deriving both the non-linear and linearized equations of motion. Colombi et al. [14] present two models, the first one relying on CR3BP dynamics and suitable for mission design, and the second one using planetary ephemerides to consider the effect of celestial bodies and solar radiation pressure perturbation and preferred for controlled dynamics: their approach also allows considering the effect of orbit-attitude coupling on relative dynamics in the cislunar environment. Franzini and Innocenti [15] develop sets of non-linear and linear differential equations for the relative motion of a spacecraft around a target object in both the restricted three-body and four-body problem formulations, the latter considering the gravitational perturbation of the Sun and the solar radiation pressure effect. As an interesting addition to their derivation, in Ref. [15] the equations of relative motion are expressed in a local-vertical-local-horizon (LVLH) frame defined by describing the target motion with respect to the Moon.

Many studies focused on the use of such dynamic models for path-planning and trajectory design, relying on some level of geometric insight or on the spectral analysis of the state matrix and numerical methods to leverage the natural dynamics of the cislunar environment. In this spirit, the analytical solutions presented by Segerman et al. [11] are expressed in terms of the amplitude and phase of motion along each Cartesian component. Elliot and Bosanac [16] also derive a set of relative motion equations in the LVLH, introducing a set of geometrical parameters for the description of quasi-periodic motions around the target and showing that they can be used as ROEs for trajectory design and path-planning. Zuehlke et al. [17, 18] use an exponential matrix model for the relative motion in CR3BP to find natural periodic solutions using a single-shooting differential correction method. Mand et al. [19] discuss preliminary trajectory design methodologies for spacecraft rendezvous around the L2 Earth-Moon Lagrange point accounting for multi-body effects, both replicating rendezvous profiles traditionally used in orbits around the Earth and introducing new approaches leveraging the unique relative dynamics around L2. Bucci et al. [20] use the spectral analysis of the state transition matrix describing the relative dynamics to identify stable and unstable manifolds and use them for mission design and guidance purposes; a similar approach is considered in Colombi et al. [14] and in Bucchioni and Innocenti [9]. However, a different perspective on relative motion modelling has been fostered using the Lyapunov-Floquet (LF) transformation, deriving from the Floquet theory for the analysis of periodic systems [21]. Given a periodic linear time-varying (LTV) system, the LF transform allows finding an equivalent linear time-invariant (LTI) system description. The LF transformation has thus proven itself to be a powerful tool to ease the handling of relative dynamics modelling and control, although its application has been investigated in few research works. Sherril et al. [22] use the LF transform to provide a mapping solution from the linearized equations of relative motion around a target in an eccentric Earth orbit to the Clohessy-Wiltshire (CW) ones. In a subsequent work [23], this transformation is used to develop a linear state-feedback controller with time-varying gains. Ogundele et al. [24] further apply the LF transformation approach to provide an approximation of the non-linear representation of the relative dynamics.

The LF transformation can also be used to enable the application of modal decomposition techniques to an LTV system. Modal decomposition allows separating the fundamental components (i.e., fundamental solutions) of a motion, such as drifting (stable or unstable) and oscillatory contributions, and express any solution as a weighted sum of such fundamental terms, which are functions of the eigenvectors and eigenvalues of the relative dynamics. The coefficients that weigh each mode of motion thus act as constants of integration and are equivalent to a set of ROEs: therefore, they carry a geometrical meaning with them concerning free relative dynamics and can be used for path-planning, guidance and control purposes. Burnett and Schaub [25-27] focus on the application of modal decomposition to different motion regimes, including the CR3BP one and highly perturbed environments, and use the coefficients of

modal decomposition as ROEs for impulsive and continuous-time path-planning. Bai et al. [28] apply the LF transformation to the relative dynamics around a target spacecraft on an eccentric Earth orbit, then retrieve the modes of motion by applying a Jordan decomposition to the state matrix of the equivalent LTI system. In doing so, they show that the initial conditions of the LTI system act as constants of integration of the motion and develop a control system that acts on such constants to perform reconfiguration maneuvers.

The work presented in this paper wishes to contribute to this research context in two ways.

- The first contribution is the development of a linearized model for the relative dynamics in cislunar environment, under the assumptions of the CR3BP and considering that the orbit of the target spacecraft is periodic. The equations of relative motion are presented in an orbiting target-fixed, velocity-based frame, in which one of the frame axes is always aligned with the instantaneous velocity vector of the target. In such a frame, if the chaser spacecraft shares the same orbit as the target one, the only motion with respect to the target that will be observed is along the flight-path direction itself. This representation relative to the current flight path is more intuitive compared to the one achieved in other orbiting frames as it is more similar to what would be observed on an elliptic orbit around the Earth.

- The second contribution fosters the application of the method of fundamental modal solutions presented by Burnett and Schaub [26, 27] to geometrically characterize the relative motion and use this result for trajectory design, guidance and control purposes. Specifically, the coefficients of modal decomposition depend on the initial conditions of motion and can be used to highlight (and design) interesting geometrical properties of the motion. Moreover, variations in the coefficients can be mathematically related to control actions that are applied to the chaser spacecraft, thus allowing the use of the coefficients as ROEs for guidance and path-planning.

The paper is articulated as follows: first, Section I.A introduces the notation and reference frames considered throughout the work. The absolute and relative dynamics are presented in Section II, which also addresses the derivation of the equations of relative motion in the velocity-based frame. At this point, the method of fundamental modal solutions decomposition is briefly recalled and the geometrical analysis of each mode of motion is conducted in Section III, in which relations are provided to bind the coefficients to the geometrical properties of the motion. The derived relative motion model and modal decomposition are then applied to specific cases of interest in Section IV, including the design of periodic, quasi-periodic, and drifting motions, and the evaluation of the impulsive ΔVs required for the execution of an approach maneuver, and the results are discussed. Finally, conclusions are drawn in Section V.

A. Notation and reference frames

In this work the following mathematical notation is considered. Scalars are indicated using italic letters (e.g., *s* or *S*). Vectors are indicated using underlined, bold italic letters (e.g., $\underline{\boldsymbol{v}}$), except for unit vectors which are simply indicated using a circumflex accent (e.g., $\hat{v}$); both are considered as column vectors by default. The norm of a vector is represented using the scalar notation but preserving the nomenclature for the vector (e.g., the norm of $\underline{\boldsymbol{v}}$ is *v*), with some exceptions highlighted throughout the paper. Matrices are indicated using bold italic letters with a double underline (e.g., $\underline{\underline{\boldsymbol{M}}}$); therefore, by extension, matrices $\underline{\underline{\boldsymbol{0}}}_n$ and $\underline{\underline{\boldsymbol{I}}}_n$ respectively represent the square null and identity matrices of order *n*. Square brackets are considered throughout the paper to specify that a physical entity is expressed in a certain frame. For example, the notation $[\underline{\boldsymbol{v}}]_a^b$ is employed to specify that the vector entity $\underline{\boldsymbol{v}}$ is observed in frame A but expressed in B. The notation simplifies to $[\underline{\boldsymbol{v}}]_b$, i.e., omitting the superscript, in case A and B are the same frame; also, it further reduces to $\underline{\boldsymbol{v}}$ in case the physical entity is considered without the need to specify in which reference frame it is observed or represented. With regards to rotation matrices, the notation $\underline{\underline{\boldsymbol{R}}}_b^a$ is employed to represent the transformation matrix that rotates vectors from frame B to frame A. Finally, with reference to angular velocity vectors, $\underline{\boldsymbol{\omega}}_{ab}$ represents the angular velocity with which frame A rotates with respect to frame B and matrix $\underline{\underline{\boldsymbol{\Omega}}}_{ab}$ represents the skew-symmetric matrix equivalent to a cross-product by vector $\underline{\boldsymbol{\omega}}_{ab}$. Moreover, the notation $[\underline{\boldsymbol{\omega}}_{ab}]^a$ and $[\underline{\underline{\boldsymbol{\Omega}}}_{ab}]^a$ is employed to specify that the components of the angular velocity are expressed in frame A. A dot notation ("ᵒ") is considered to express differentiation with respect to time; multiple dots imply that differentiation occurs multiple times. Finally, dimensional quantities are represented using the symbol "ᵒ": if not specified, the considered quantity is dimensionless.

This notation approach is employed to deal with vectors being observed from multiple reference frames that rotate one with respect to another. An example of application of this notation is provided as a clarification. Let us consider two frames A and B, with frame B being a non-inertial reference frame rotating with respect to A with angular velocity $\underline{\boldsymbol{\omega}}_{ba}$ and with vectors $\underline{\boldsymbol{\rho}}$ and $\dot{\underline{\boldsymbol{\rho}}}$ defining the position and velocity of the origin of frame B with respect to A; then, let a

particle have position vectors $\underline{r}$ and $\underline{r}'$ in frames A and B, respectively. Recalling that position vectors represent the same physical entity regardless of the reference frame they are observed in, the velocity of the particle in frame A can thus be expressed as in Eq. (1) by applying the transport theorem:

$$\left[\dot{\underline{r}}\right]_a = \left[\dot{\underline{\rho}}\right]_a + \left[\dot{\underline{r}}'\right]_a = \left[\dot{\underline{\rho}}\right]_a + \left[\dot{\underline{r}}'\right]_b^a + \left[\underline{\omega}_{ba}\right]^a \times \left[\underline{r}'\right]_a = \left[\dot{\underline{\rho}}\right]_a + \left[\dot{\underline{r}}'\right]_b^a + \left[\underline{\underline{\Omega}}_{ba}\right]^a \left[\underline{r}'\right]_a \tag{1}$$

To present the equations of relative motion, first an inertial reference frame (IRF) is defined, indicated using letter "I", where the motion of the Earth and Moon is taking place. Considering the origin of the reference frame in the barycenter B of the system of the two primary bodies (Earth and Moon), it is then defined as $\{B, \hat{I}, \hat{J}, \hat{K}\}$ and its axes are aligned with those of the classical Earth-centered inertial frame. The CR3BP equations are usually expressed in the synodal barycentric reference frame, centered in B with its x axis pointing towards the Moon, its z axis aligned with the angular velocity of the rotation of the primaries around their barycenter, and the y axis completing the right-handed frame. In this work, a Moon-centered, x/y inverted synodal frame (MRF) is defined as $\{M, \hat{x}_{MRF}, \hat{y}_{MRF}, \hat{z}_{MRF}\}$, indicated with letter "M", with its origin in the Moon, the x axis instantaneously pointing towards the Earth, the z axis parallel to the angular velocity of rotation of the Earth-Moon system with respect to the IRF, $\underline{\omega}_{mi}$, and the y axis completing the right handed frame. It is worth noting that the MRF is considered in this work alternatively to the synodal barycentric reference frame, compared to which a change in origin and an inversion in the x and y axes occur. This choice is inherited from the work of Franzini and Innocenti [15] as it allows defining an orbiting reference frame for cislunar orbits as if the Moon were the central body, similarly to how it would be defined in an Earth-centered orbit. The choice of the Moon as the origin of the MRF is thus only related to the fact that the cislunar orbits considered in this work are closer to the Moon. Finally, the orbiting reference frame in which the relative motion equations will be developed is defined as a velocity frame (VRF) [29], represented as $\{V, \hat{i}, \hat{j}, \hat{k}\}$ and indicated with letter "V", with its origin in the target spacecraft, the y axis aligned with the instantaneous velocity vector, the z axis aligned with the instantaneous angular momentum vector, and the x axis completing the right-handed frame. A graphical representation of the reference frames discussed so far and how are they related one to another is provided in Fig. 1.
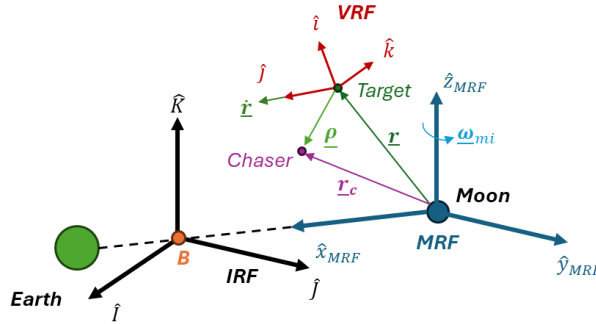

Fig. 1 Graphical representation of the reference frames and their relationship.

II. Dynamics in the circular restricted three-body problem

In this work, the absolute motion of the target spacecraft is assumed to be described by CR3BP equations, in which periodic or quasi-periodic orbits for the target spacecraft can be found. However, this choice does not limit the validity of the proposed methodology: in fact, when the state-space formulation of the relative dynamics will be presented, it will be shown that a change in the absolute dynamics would only affect how the state matrix of the system is computed. Clearly, the corresponding initial conditions need to be corrected to maintain the property of (quasi-)periodicity outside of CR3BP assumptions. Therefore, first the equations of the CR3BP formulation will be recalled for the sake of completeness; then, the equations of the relative motion will be derived.

A. Absolute motion in the CR3BP

The vector equation of the three-body problem representing the motion of the spacecraft with respect to the Moon can be expressed in dimensional quantities in the IRF under the restriction assumption as in Eq. (2), where $\underline{r}$ represents

the position vector of the spacecraft, $\underline{r}_{em}$ is the position vector of the Moon with respect to the Earth, $\overline{\mu}_e$ and $\overline{\mu}_m$ are the gravitational parameters of Earth and Moon.

$$\left[\ddot{\overline{\underline{r}}}\right]_i = -\overline{\mu}_m \frac{\left[\overline{\underline{r}}\right]_i}{\overline{r}^3} - \overline{\mu}_e \left(\frac{\left[\overline{\underline{r}} + \overline{\underline{r}}_{em}\right]_i}{\left\|\overline{\underline{r}} + \overline{\underline{r}}_{em}\right\|^3} - \frac{\left[\overline{\underline{r}}_{em}\right]_i}{\overline{r}_{em}^3} \right) \tag{2}$$

The circularization hypothesis implies that the Moon revolves on a circular orbit around the Earth. The equations of the CR3BP are usually reported in their dimensionless form, which is obtained by: (*i*) imposing that the sum of the dimensionless masses of the primaries equals unity (or, equivalently, that the sum of their dimensionless gravitational parameters equals unity); (*ii*) the sum of the dimensionless distances of the primaries from their barycenter equals unity, i.e., $r_{em} = 1$; and (*iii*) the time unit of the system is the inverse of the synodal frequency $\overline{\omega}_{mi}$. As a result of the latter, the dimensionless synodal frequency equals unity. Equation (3) reports the dimensionless form of the CR3BP equations in the MRF, where μ is the dimensionless ratio between the gravitational parameters, and because of the use of the MRF, $[\underline{r}_{em}]_m = [-1, 0, 0]^T$. Equation (4) reports the relationship between dimensionless and dimensional quantities.

$$\left[\ddot{\underline{r}}\right]_m = -2\left[\underline{\underline{\Omega}}_{mi}\right]^m \left[\dot{\underline{r}}\right]_m - \left[\underline{\underline{\Omega}}_{mi}^2\right]^m \left[\underline{r}\right]_m - \mu \frac{\left[\underline{r}\right]_m}{r^3} - (1-\mu) \frac{\left[\underline{r} + \underline{r}_{em}\right]_m}{\left\|\underline{r} + \underline{r}_{em}\right\|^3} \tag{3}$$

$$\mu = \frac{\overline{\mu}_m/\overline{\mu}_e}{1 + \overline{\mu}_m/\overline{\mu}_e}, \quad \overline{t} = \frac{t}{\overline{\omega}_{mi}}, \quad \overline{\underline{r}} = \overline{r}_{em}\underline{r}, \quad \dot{\overline{\underline{r}}} = \overline{\omega}_{mi}\overline{r}_{em}\dot{\underline{r}}, \quad \ddot{\overline{\underline{r}}} = \overline{\omega}_{mi}^2\overline{r}_{em}\ddot{\underline{r}}, \quad \overline{\omega}_{mi} = \sqrt{\frac{\overline{\mu}_e + \overline{\mu}_m}{\overline{r}_{em}^3}} \tag{4}$$

The CR3BP assumptions thus introduce a simplification of the actual motion occurring between the two primaries to reduce the complexity of the equations. In this respect, these equations would be ideal for on board online guidance purposes compared to more accurate sets of equations (e.g., the elliptical restricted three-body problem equations, or the full ephemeris restricted four-body problem equations) because of their mathematical simplicity. However, Franzini and Innocenti [15] highlight their suitability for GNC applications only at the aposelene: therefore, the CR3BP assumptions will be considered in this work to develop the proposed methodology, but further work will be required in the future to generalize the methodology to other regimes of the cislunar environment.

B. Derivation of relative motion equations in VRF

The derivation of the relative motion equations in VRF follows a similar approach to the one adopted by Franzini and Innocenti [15]. First, the relative position vector $\underline{\rho}$ of the chaser with respect to the target is defined as in Eq. (5) where *x*, *y*, and *z* are its components in VRF, and $\underline{r}_c$ and $\underline{r}$ are the position vectors of the chaser and the target.

$$\left[\underline{\rho}\right]_i = \left[\underline{r}_c\right]_i - \left[\underline{r}\right]_i = x[\hat{\imath}]_i + y[\hat{\jmath}]_i + z[\hat{k}]_i \tag{5}$$

By differentiating Eq. (5) two times, the relative acceleration between the target and the chaser can be related to its expression in the VRF frame through the transport theorem as follows:

$$\left[\dot{\underline{\rho}}\right]_i = \left[\dot{\underline{r}}_c\right]_i - \left[\dot{\underline{r}}\right]_i = \left[\dot{\underline{\rho}}\right]_v^i + \left[\underline{\underline{\Omega}}_{vi}\right]^i \left[\underline{\rho}\right]_i \tag{6}$$

$$\left[\ddot{\underline{\rho}}\right]_i = \left[\ddot{\underline{r}}_c\right]_i - \left[\ddot{\underline{r}}\right]_i = \left[\ddot{\underline{\rho}}\right]_v^i + 2\left[\underline{\underline{\Omega}}_{vi}\right]^i \left[\dot{\underline{\rho}}\right]_v^i + \left[\underline{\dot{\underline{\Omega}}}_{vi}\right]_v^i \left[\underline{\rho}\right]_i + \left[\underline{\underline{\Omega}}_{vi}^2\right]^i \left[\underline{\rho}\right]_i \tag{7}$$

Substituting terms $[\ddot{\underline{r}}]_i$ and $[\ddot{\underline{r}}_c]_i$ in Eq. (7) as per Eq. (2), the non-linear equations of relative motion as observed in the VRF are obtained. These are reported in Eq. (8 considering that the angular velocity of the VRF with respect to the IRF and its derivative in time can be computed as per Eqs. (9)-(10).

$$\left[\ddot{\underline{\rho}}\right]_v^i + 2\left[\underline{\underline{\Omega}}_{vi}\right]^i \left[\dot{\underline{\rho}}\right]_v^i + \left[\underline{\dot{\underline{\Omega}}}_{vi}\right]_v^i \left[\underline{\rho}\right]_i + \left[\underline{\underline{\Omega}}_{vi}^2\right]^i \left[\underline{\rho}\right]_i =$$
$$= \mu \left(\frac{\left[\underline{r}\right]_i}{r^3} - \frac{\left[\underline{r} + \underline{\rho}\right]_i}{\left\|\underline{r} + \underline{\rho}\right\|^3} \right) + (1-\mu) \left(\frac{\left[\underline{r} + \underline{r}_{em}\right]_i}{\left\|\underline{r} + \underline{r}_{em}\right\|^3} - \frac{\left[\underline{r} + \underline{r}_{em} + \underline{\rho}\right]_i}{\left\|\underline{r} + \underline{r}_{em} + \underline{\rho}\right\|^3} \right) \tag{8}$$

$$\underline{\boldsymbol{\omega}}_{vi} = \underline{\boldsymbol{\omega}}_{vm} + \underline{\boldsymbol{\omega}}_{mi} \tag{9}$$

$$\left[\underline{\dot{\boldsymbol{\omega}}}_{vi}\right]_v^i = \left[\underline{\dot{\boldsymbol{\omega}}}_{vm}\right]_v^i + \left[\underline{\dot{\boldsymbol{\omega}}}_{mi}\right]_v^i = \left[\underline{\dot{\boldsymbol{\omega}}}_{vm}\right]_v^i + \left[\underline{\dot{\boldsymbol{\omega}}}_{mi}\right]_m^i - \left[\underline{\boldsymbol{\Omega}}_{vm}\right]^i \left[\underline{\boldsymbol{\omega}}_{mi}\right]^i \tag{10}$$

The angular velocity and acceleration vectors $\underline{\boldsymbol{\omega}}_{vi}$ and $\underline{\dot{\boldsymbol{\omega}}}_{vi}$ are thus functions of both the angular motion of the MRF with respect to the IRF and the angular motion of the VRF with respect to the MRF. As also explained in Ref. [15], the quantities considered in Eqs. (9) and (10) can be expressed in analytical form. In fact, while $\underline{\boldsymbol{\omega}}_{mi}$ and $\underline{\dot{\boldsymbol{\omega}}}_{mi}$ are constant quantities within the CR3BP formulation and equal to $\underline{\boldsymbol{\omega}}_{mi} = [0, 0, 1]^T$ and $\underline{\dot{\boldsymbol{\omega}}}_{mi} = [0, 0, 0]^T$ respectively, $\underline{\boldsymbol{\omega}}_{vm}$ and $\underline{\dot{\boldsymbol{\omega}}}_{vm}$ can instead be computed based on the knowledge of the state of the target spacecraft in the MRF. From the definition of the unit vectors of the VRF axes provided in Eq. (11), where v and h are the norms of vectors $[\underline{\dot{\boldsymbol{r}}}]_m^i$ and $[\underline{\boldsymbol{r}}]_i \times [\underline{\dot{\boldsymbol{r}}}]_m^i$, respectively, the transport theorem can be applied to obtain a relationship between their time derivatives observed in MRF and $\underline{\boldsymbol{\omega}}_{vm}$ as in Eq. (12) (see details in Ref. [15]).

$$[\hat{\imath}]_i = [\hat{\jmath}]_i \times [\hat{k}]_i, \qquad [\hat{\jmath}]_i = \frac{[\underline{\dot{\boldsymbol{r}}}]_m^i}{\left\|[\underline{\dot{\boldsymbol{r}}}]_m^i\right\|} = \frac{[\underline{\dot{\boldsymbol{r}}}]_m^i}{v}, \qquad [\hat{k}]_i = \frac{[\underline{\boldsymbol{h}}]_m^i}{h} = \frac{[\underline{\boldsymbol{r}}]_i \times [\underline{\dot{\boldsymbol{r}}}]_m^i}{\left\|[\underline{\boldsymbol{r}}]_i \times [\underline{\dot{\boldsymbol{r}}}]_m^i\right\|} \tag{11}$$

$$[\hat{\imath}]_i \times [\hat{\imath}]_m^i + [\hat{\jmath}]_i \times [\hat{\jmath}]_m^i + [\hat{k}]_i \times [\hat{k}]_m^i = 2[\underline{\boldsymbol{\omega}}_{vm}]^i \tag{12}$$

Therefore, explicitly evaluating vectors $[\hat{\imath}]_m^i$, $[\hat{\jmath}]_m^i$ and $[\hat{k}]_m^i$ allows to find analytical expressions for the components of $\underline{\boldsymbol{\omega}}_{vm}$ directly in the VRF [15]. Once vector $\underline{\boldsymbol{\omega}}_{vm}$ is found, its components can be derived to find the corresponding angular acceleration as expressed in the VRF. Based on Eq. (11), unit vector $[\hat{\jmath}]_m^i$ can be computed as follows:

$$[\hat{\jmath}]_m^i = \frac{[\underline{\ddot{\boldsymbol{r}}}]_m^i v - [\underline{\dot{\boldsymbol{r}}}]_m^i \dot{v}}{v^2} = \frac{1}{v}\left([\underline{\ddot{\boldsymbol{r}}}]_m^i - \dot{v}[\hat{\jmath}]_i\right) = \frac{1}{v}\left\{\left([\underline{\ddot{\boldsymbol{r}}}]_m^i \cdot [\hat{\imath}]_i\right)[\hat{\imath}]_i + \left([\underline{\ddot{\boldsymbol{r}}}]_m^i \cdot [\hat{k}]_i\right)[\hat{k}]_i\right\} \tag{13}$$

where $\dot{v}$ is the projection of the acceleration vector along the y axis of the VRF:

$$\dot{v} = [\underline{\ddot{\boldsymbol{r}}}]_v^i \cdot [\hat{\jmath}]_i = \left([\underline{\ddot{\boldsymbol{r}}}]_m^i - [\underline{\boldsymbol{\Omega}}_{vm}]^i [\underline{\dot{\boldsymbol{r}}}]_m^i\right) \cdot [\hat{\jmath}]_i = [\underline{\ddot{\boldsymbol{r}}}]_m^i \cdot [\hat{\jmath}]_i \tag{14}$$

Similarly, vector $[\hat{k}]_m^i$ can be expressed as:

$$[\hat{k}]_m^i = \frac{[\underline{\dot{\boldsymbol{h}}}]_m^i - \dot{h}[\hat{k}]_i}{h} = \frac{1}{h}\left\{[\underline{\dot{\boldsymbol{h}}}]_m^i - \left([\underline{\dot{\boldsymbol{h}}}]_m^i \cdot [\hat{k}]_i\right)[\hat{k}]_i\right\} = \frac{1}{h}\left\{\left([\underline{\dot{\boldsymbol{h}}}]_m^i \cdot [\hat{\imath}]_i\right)[\hat{\imath}]_i + \left([\underline{\dot{\boldsymbol{h}}}]_m^i \cdot [\hat{\jmath}]_i\right)[\hat{\jmath}]_i\right\} \tag{15}$$

where $\dot{h}$ is the projection of the time derivative of the orbit angular momentum vector along the z axis of the VRF:

$$\dot{h} = [\underline{\dot{\boldsymbol{h}}}]_v^i \cdot [\hat{k}]_i = \left([\underline{\dot{\boldsymbol{h}}}]_m^i - [\underline{\boldsymbol{\Omega}}_{vm}]^i [\underline{\boldsymbol{h}}]_v^i\right) \cdot [\hat{k}]_i = [\underline{\dot{\boldsymbol{h}}}]_m^i \cdot [\hat{k}]_i \tag{16}$$

As a result, applying the rule of the derivative of a product to the expression of $[\hat{\imath}]_i$ in Eq. (11) and substituting Eqs. (13) and (15), the following result is obtained:

$$[\hat{\imath}]_m^i = [\hat{\jmath}]_m^i \times [\hat{k}]_i - [\hat{k}]_m^i \times [\hat{\jmath}]_i = -\frac{1}{v}\left([\underline{\ddot{\boldsymbol{r}}}]_m^i \cdot [\hat{\imath}]_i\right)[\hat{\jmath}]_i - \frac{1}{h}\left([\underline{\dot{\boldsymbol{h}}}]_m^i \cdot [\hat{\imath}]_i\right)[\hat{k}]_i \tag{17}$$

Equations (13)-(17) provide an expression of the derivatives of the directions of the VRF expressed in terms of the components of such variations along the axes of the VRF itself. Combining these results in Eq. (12), an expression of $\underline{\boldsymbol{\omega}}_{vm}$ in terms of its components along the axes of the VRF is obtained, as reported in Eq. (18).

$$[\underline{\boldsymbol{\omega}}_{vm}]^i = \left(\frac{1}{2v}[\underline{\ddot{\boldsymbol{r}}}]_m^i \cdot [\hat{k}]_i - \frac{1}{2h}[\underline{\dot{\boldsymbol{h}}}]_m^i \cdot [\hat{\jmath}]_i\right)[\hat{\imath}]_i + \left(\frac{1}{h}[\underline{\dot{\boldsymbol{h}}}]_m^i \cdot [\hat{\imath}]_i\right)[\hat{\jmath}]_i + \left(-\frac{1}{v}[\underline{\ddot{\boldsymbol{r}}}]_m^i \cdot [\hat{\imath}]_i\right)[\hat{k}]_i \tag{18}$$

The components of $\underline{\boldsymbol{\omega}}_{vm}$ along the axes of the VRF can be developed further from Eq. (18) by explicating the dot products. Borrowing the following definition of $\dot{r}$ from Ref. [15], which considers $\dot{r}$ as the projection of the velocity vector along the radial direction (identified by the direction of the position vector of the target):

6

$$\dot{r} = \frac{1}{r}\left[\underline{\boldsymbol{r}}\right]_i \cdot \left[\underline{\dot{\boldsymbol{r}}}\right]_m^i \tag{19}$$

the dot products in Eq. (18) can be explicated as follows:

$$\left[\underline{\ddot{\boldsymbol{r}}}\right]_m^i \cdot [\hat{\imath}]_i = \left[\underline{\ddot{\boldsymbol{r}}}\right]_m^i \cdot \left([\hat{\jmath}]_i \times [\hat{k}]_i\right) = \left[\underline{\ddot{\boldsymbol{r}}}\right]_m^i \cdot \left(\frac{\left[\underline{\dot{\boldsymbol{r}}}\right]_m^i}{v} \times \frac{\left[\underline{\boldsymbol{h}}\right]_m^i}{h}\right) =$$

$$= \frac{1}{hv}\left[\underline{\ddot{\boldsymbol{r}}}\right]_m^i \cdot \left\{\left(\left[\underline{\dot{\boldsymbol{r}}}\right]_m^i \cdot \left[\underline{\dot{\boldsymbol{r}}}\right]_m^i\right)\left[\underline{\boldsymbol{r}}\right]_i - \left(\left[\underline{\dot{\boldsymbol{r}}}\right]_m^i \cdot \left[\underline{\boldsymbol{r}}\right]_i\right)\left[\underline{\dot{\boldsymbol{r}}}\right]_m^i\right\} = \tag{20}$$

$$= \frac{v}{h}\left(\left[\underline{\ddot{\boldsymbol{r}}}\right]_m^i \cdot \left[\underline{\boldsymbol{r}}\right]_i\right) - \frac{r\dot{r}}{hv}\left(\left[\underline{\ddot{\boldsymbol{r}}}\right]_m^i \cdot \left[\underline{\dot{\boldsymbol{r}}}\right]_m^i\right)$$

$$\left[\underline{\ddot{\boldsymbol{r}}}\right]_m^i \cdot [\hat{k}]_i = \left[\underline{\ddot{\boldsymbol{r}}}\right]_m^i \cdot \frac{\left[\underline{\boldsymbol{h}}\right]_m^i}{h} = \frac{1}{h}\left[\underline{\ddot{\boldsymbol{r}}}\right]_m^i \cdot \left(\left[\underline{\boldsymbol{r}}\right]_i \times \left[\underline{\dot{\boldsymbol{r}}}\right]_m^i\right) \tag{21}$$

$$\left[\underline{\dot{\boldsymbol{h}}}\right]_m^i \cdot [\hat{\imath}]_i = \left(\left[\underline{\boldsymbol{r}}\right]_i \times \left[\underline{\dot{\boldsymbol{r}}}\right]_m^i\right) \cdot \left([\hat{\jmath}]_i \times [\hat{k}]_i\right) =$$

$$= \left(\left[\underline{\boldsymbol{r}}\right]_i \cdot [\hat{\jmath}]_i\right)\left(\left[\underline{\dot{\boldsymbol{r}}}\right]_m^i \cdot [\hat{k}]_i\right) - \left(\left[\underline{\boldsymbol{r}}\right]_i \cdot [\hat{k}]_i\right)\left(\left[\underline{\dot{\boldsymbol{r}}}\right]_m^i \cdot [\hat{\jmath}]_i\right) = \frac{r\dot{r}}{hv}\left[\underline{\dot{\boldsymbol{r}}}\right]_m^i \cdot \left[\underline{\boldsymbol{h}}\right]_m^i \tag{22}$$

$$\left[\underline{\dot{\boldsymbol{h}}}\right]_m^i \cdot [\hat{\jmath}]_i = \left(\left[\underline{\boldsymbol{r}}\right]_i \times \left[\underline{\dot{\boldsymbol{r}}}\right]_m^i\right) \cdot \frac{\left[\underline{\dot{\boldsymbol{r}}}\right]_m^i}{v} = -\frac{1}{v}\left[\underline{\dot{\boldsymbol{r}}}\right]_m^i \cdot \left[\underline{\boldsymbol{h}}\right]_m^i \tag{23}$$

As a result, by substituting Eqs. (20)-(23) into Eq. (18), the components $\omega_{vm,x}^v$, $\omega_{vm,y}^v$, and $\omega_{vm,z}^v$ of vector $\underline{\boldsymbol{\omega}}_{vm}$ along the VRF axes can be obtained as a function of quantities related to the absolute motion of the target object. These are shown in Eq. (24).

$$\left[\underline{\boldsymbol{\omega}}_{vm}\right]^v = \begin{cases} \omega_{vm,x}^v = \dfrac{1}{hv}\left[\underline{\ddot{\boldsymbol{r}}}\right]_m^i \cdot \left[\underline{\boldsymbol{h}}\right]_m^i \\[2mm] \omega_{vm,y}^v = \dfrac{r\dot{r}}{h^2 v}\left[\underline{\ddot{\boldsymbol{r}}}\right]_m^i \cdot \left[\underline{\boldsymbol{h}}\right]_m^i \\[2mm] \omega_{vm,z}^v = -\dfrac{1}{h}\left[\underline{\ddot{\boldsymbol{r}}}\right]_m^i \cdot \left[\underline{\boldsymbol{r}}\right]_i + \dfrac{r\dot{r}}{hv^2}\left[\underline{\ddot{\boldsymbol{r}}}\right]_m^i \cdot \left[\underline{\dot{\boldsymbol{r}}}\right]_m^i \end{cases} \tag{24}$$

By directly differentiating the VRF components of vector $\underline{\boldsymbol{\omega}}_{vm}$, the components $\dot{\omega}_{vm,x}^v$, $\dot{\omega}_{vm,y}^v$, and $\dot{\omega}_{vm,z}^v$ of vector $\underline{\dot{\boldsymbol{\omega}}}_{vm}$ expressed in the same frame can be obtained. The direct differentiation yields:

$$\left[\underline{\dot{\boldsymbol{\omega}}}_{vm}\right]_v = \begin{cases} \dot{\omega}_{vm,x}^v = -\left(\dfrac{\dot{h}}{h} + \dfrac{\dot{v}}{v}\right)\omega_{vm,x}^v + \dfrac{1}{hv}\left[\underline{\dddot{\boldsymbol{r}}}\right]_m^i \cdot \left[\underline{\boldsymbol{h}}\right]_m^i \\[3mm] \dot{\omega}_{vm,y}^v = \left(\dfrac{\dot{r}}{r} - \dfrac{\dot{v}}{v} - \dfrac{2\dot{h}}{h}\right)\omega_{vm,y}^v + \dfrac{r\ddot{r}}{h}\omega_{vm,x}^v + \dfrac{r\dot{r}}{h^2 v}\left[\underline{\dddot{\boldsymbol{r}}}\right]_m^i \cdot \left[\underline{\boldsymbol{h}}\right]_m^i \\[3mm] \dot{\omega}_{vm,z}^v = -\dfrac{\dot{h}}{h}\omega_{vm,z}^v - \dfrac{1}{h}\left[\underline{\dddot{\boldsymbol{r}}}\right]_m^i \cdot \left[\underline{\boldsymbol{r}}\right]_i + \\[3mm] + \left\{\left(\dfrac{\dot{r}}{r} - \dfrac{2\dot{v}}{v}\right)\dfrac{r\dot{r}}{hv^2} + \dfrac{r\ddot{r}}{hv^2} - \dfrac{1}{h}\right\}\left[\underline{\ddot{\boldsymbol{r}}}\right]_m^i \cdot \left[\underline{\dot{\boldsymbol{r}}}\right]_m^i + \dfrac{r\dot{r}}{hv^2}\left(\left[\underline{\dddot{\boldsymbol{r}}}\right]_m^i \cdot \left[\underline{\dot{\boldsymbol{r}}}\right]_m^i + \left\|\left[\underline{\ddot{\boldsymbol{r}}}\right]_m^i\right\|^2\right) \end{cases} \tag{25}$$

in which $\ddot{r}$ can be obtained by directly differentiating $\dot{r}$ as follows:

$$\ddot{r} = \frac{\partial \dot{r}}{\partial t} = \frac{1}{r}\left(v^2 + \left[\underline{\boldsymbol{r}}\right]_i \cdot \left[\underline{\ddot{\boldsymbol{r}}}\right]_m^i - \dot{r}^2\right) \tag{26}$$

and the jerk term $\left[\underline{\dddot{\boldsymbol{r}}}\right]_m^i$ can be obtained by direct derivation of the target acceleration expressed as in Eq. (3), with the useful notation for the derivative of the terms $\underline{\boldsymbol{p}}/p^3$ borrowed by Ref. [15]:

7

$$\left[\ddot{\boldsymbol{r}}\right]_m^i = -2\left[\underline{\boldsymbol{\Omega}}_{mi}\right]^i \left[\ddot{\boldsymbol{r}}\right]_m^i - \left[\underline{\boldsymbol{\Omega}}_{mi}^2\right]^i \left[\dot{\boldsymbol{r}}\right]_m^i - \mu \frac{\partial}{\partial \underline{\boldsymbol{r}}}\left[\frac{[\boldsymbol{r}]_i}{r^3}\right]\left[\dot{\boldsymbol{r}}\right]_m^i - (1-\mu)\frac{\partial}{\partial \underline{\boldsymbol{r}}}\left[\frac{[\boldsymbol{r}+\boldsymbol{r}_{em}]_i}{\|\underline{\boldsymbol{r}}+\underline{\boldsymbol{r}}_{em}\|^3}\right]\left[\dot{\boldsymbol{r}}\right]_m^i \ ,$$

$$\frac{\partial}{\partial \underline{\boldsymbol{p}}}\left[\frac{\underline{\boldsymbol{p}}}{p^3}\right] = \frac{1}{p^3}\left(\underline{\boldsymbol{I}}_3 - 3\frac{\underline{\boldsymbol{p}}\,\underline{\boldsymbol{p}}^T}{p^2}\right) \tag{27}$$

Once the components of the angular velocity and angular acceleration vectors of the VRF with respect to the MRF have been computed, they can be substituted into Eqs. (8)-(10) to achieve a non-linear description of the relative motion. However, when the chaser and target spacecraft are sufficiently close one to another, i.e., for $\rho/r << 1$, a linearization can be conducted about the orbit $\underline{r}(t)$ of the target spacecraft. This yields to the following linearized equations of relative motion in the velocity frame:

$$\left[\ddot{\boldsymbol{\rho}}\right]_v + 2\left[\underline{\boldsymbol{\Omega}}_{vi}\right]^v \left[\dot{\boldsymbol{\rho}}\right]_v + \left[\dot{\underline{\boldsymbol{\Omega}}}_{vi}\right]_v \left[\boldsymbol{\rho}\right]_v + \left[\underline{\boldsymbol{\Omega}}_{vi}^2\right]^v \left[\boldsymbol{\rho}\right]_v =$$
$$= -\frac{\mu}{r^3}\left(\underline{\boldsymbol{I}}_3 - 3\frac{[\boldsymbol{r}]_v[\boldsymbol{r}]_v^T}{r^2}\right)\left[\boldsymbol{\rho}\right]_v - \frac{(1-\mu)}{\|\underline{\boldsymbol{r}}+\underline{\boldsymbol{r}}_{em}\|^3}\left(\underline{\boldsymbol{I}}_3 - 3\frac{[\boldsymbol{r}+\boldsymbol{r}_{em}]_v[\boldsymbol{r}+\boldsymbol{r}_{em}]_v^T}{\|\underline{\boldsymbol{r}}+\underline{\boldsymbol{r}}_{em}\|^2}\right)\left[\boldsymbol{\rho}\right]_v \tag{28}$$

As a last remark, it is useful to rewrite Eq. (28) in the form of a linear time-varying (LTV) system as shown in Eq. (29), in which the state vector is defined as $\underline{x} = [[\boldsymbol{\rho}]_v{}^T, [\dot{\boldsymbol{\rho}}]_v{}^T]^T$, and the input vector $\underline{u}$ has its components expressed along the VRF axes.

$$\underline{\dot{x}} = \underline{\underline{A}}(t)\,\underline{x} + \underline{\underline{B}}\,\underline{u}, \qquad \underline{\underline{A}}(t) = \begin{bmatrix} \underline{\underline{0}}_3 & \underline{\underline{I}}_3 \\ \underline{\underline{A}}_v(t) & -2\left[\underline{\boldsymbol{\Omega}}_{vi}(t)\right]^v \end{bmatrix}, \qquad \underline{\underline{B}} = \begin{bmatrix} \underline{\underline{0}}_3 \\ \underline{\underline{I}}_3 \end{bmatrix} \tag{29}$$

$$\underline{\underline{A}}_v(t) = -\left[\dot{\underline{\boldsymbol{\Omega}}}_{vi}\right]_v - \left[\underline{\boldsymbol{\Omega}}_{vi}^2\right]^v - \frac{\mu}{r^3}\left(\underline{\underline{I}}_3 - 3\frac{[\boldsymbol{r}]_v[\boldsymbol{r}]_v^T}{r^2}\right) - \frac{(1-\mu)}{\|\underline{\boldsymbol{r}}+\underline{\boldsymbol{r}}_{em}\|^3}\left(\underline{\underline{I}}_3 - 3\frac{[\boldsymbol{r}+\boldsymbol{r}_{em}]_v[\boldsymbol{r}+\boldsymbol{r}_{em}]_v^T}{\|\underline{\boldsymbol{r}}+\underline{\boldsymbol{r}}_{em}\|^2}\right) \tag{30}$$

Matrix $\underline{\underline{A}}(t)$ is the Jacobian of Eq. (28) and it strictly depends on the absolute dynamics of the target spacecraft. Moreover, if the target orbit is periodic, $\underline{\underline{A}}(t)$ will show the same periodicity: therefore, Eqs. (29) and (30) represent a periodic LTV system if the orbit of the target spacecraft is periodic. This formulation also allows introducing more complex assumptions of the motion if the elements of the matrix are modified accordingly (e.g., by introducing the gravitational acceleration of a fourth body or the solar radiation pressure acceleration in $\underline{\underline{A}}_v$ or as part of the input $\underline{u}$ [13]), as long as the linearization remains valid.

III. Modal decomposition of the relative motion in the CR3BP

The relative motion between two spacecraft in the CR3BP is particularly complicated, and like the absolute one it has some special analytical solutions [11] but not a general one. To gain further insight into its properties, the method of fundamental modal solutions presented in Ref. [26, 27] is here applied to the VRF formulation derived in the previous section and reported in Eqs. (29) and (30) as a periodic LTV system. Clearly, this is possible if a proper LF transformation is identified to get an equivalent LTI system first.

A. Mathematical background

Given a periodic LTV system with period T in the form provided in Eq. (29), the equation obtained by considering a null forcing term describes the natural evolution of the system. The same equation can be rewritten in matrix form as in Eq. (31), in which matrix $\underline{\underline{\Phi}}(t, t_0)$ represents the state transition matrix (STM) of the system from an initial time, t_0, to a given time, t, and it is such that $\underline{\underline{\Phi}}(t_0, t_0) = \underline{\underline{I}}_6$. Equation (31) is known as the fundamental matrix equation, defining how the STM propagates over time, and Eq. (32) provides a solution to it.

$$\underline{\underline{\dot{\Phi}}}(t, t_0) = \underline{\underline{A}}(t)\underline{\underline{\Phi}}(t, t_0) \tag{31}$$

$$\underline{\underline{\Phi}}(t, t_0) = \underline{\underline{P}}(t)e^{\underline{\underline{\Lambda}}(t-t_0)} \tag{32}$$

8

In Eq. (32), matrix $\underline{\underline{\Delta}}$ has complex entries and it is constant over time, while matrix $\underline{\underline{P}}(t)$ is the LF transformation matrix, which must satisfy the following matrix equation [26, 27]:

$$\underline{\underline{P}}^{-1}(t)\left(\underline{\underline{A}}(t)\underline{\underline{P}}(t) - \underline{\underline{\dot{P}}}(t)\right) = \underline{\underline{\Delta}}(t) \tag{33}$$

Many solutions exist to the differential equation (33) in $\underline{\underline{P}}(t)$: in accordance with previous works [25-28], the solution considered in this work is shown in Eq. (34) and is obtained by inverting Eq. (32), yielding a periodic matrix with period T and equal to the identity matrix at time t_0.

$$\underline{\underline{P}}(t) = \underline{\underline{\Phi}}(t, t_0)e^{-\underline{\underline{\Delta}}(t-t_0)}, \qquad \underline{\underline{P}}(t_0) = \underline{\underline{P}}(t_0 + T) = \underline{\underline{I}}_6 \tag{34}$$

Equation (34) provides a way of computing matrix $\underline{\underline{P}}(t)$, although this requires knowing matrix $\underline{\underline{\Delta}}$ first. To compute the latter, it must be recalled that in LTV systems matrix $\underline{\underline{\Phi}}(t_0 + T, t_0) = \underline{\underline{M}}$ is known as the monodromy matrix of the system. Evaluating Eq. (32) at time $t_0 + T$ and inverting it allows computing matrix $\underline{\underline{\Delta}}$ from matrix $\underline{\underline{M}}$ as per Eq. (35), where the natural logarithm of a matrix is defined as the principal matrix logarithm (i.e., the inverse transformation of the matrix exponential).

$$\underline{\underline{M}} = \underline{\underline{P}}(t_0 + T)e^{\underline{\underline{\Delta}}T} = \underline{\underline{I}}_6 e^{\underline{\underline{\Delta}}T} \quad \Rightarrow \quad \underline{\underline{\Delta}} = \frac{1}{T}\ln\underline{\underline{M}} \tag{35}$$

In complicated dynamics systems such as the one considered in this work, numerically integrating Eq. (31) over a full period T allows determining the evolution of the STM over interval $[t_0, t_0 + T]$ and the monodromy matrix $\underline{\underline{M}}$. At this point, Eq. (35) is employed to compute matrix $\underline{\underline{\Delta}}$, and Eq. (34) can be used to compute matrix $\underline{\underline{P}}(t)$ over a period. As a result, the following LF transformation can be defined between the LTV state $\underline{x}$ and the LTI state $\underline{z}$, representing an instantaneous change of coordinates between the original LTV system and the equivalent LTI system of Eq. (37). In the latter, the first term in the right-hand side of the equation is the direct transformation of the homogeneous equation of the LTV system and the second term directly results from Eq. (29) when the coordinate transformation in Eq. (36) is applied [28]. It must be noted that, equivalently, Eq. (37) can be obtained by directly applying the transformation in Eq. (36) to Eq. (29) and considering that Eq. (33) defines matrix $\underline{\underline{\Delta}}$.

$$\underline{x}(t) = \underline{\underline{P}}(t)\underline{z}(t) \tag{36}$$

$$\underline{\dot{z}} = \underline{\underline{\Lambda}}\,\underline{z} + \underline{\underline{P}}^{-1}(t)\underline{\underline{B}}\,\underline{u} \tag{37}$$

The modal decomposition is finally applied to the equivalent LTI system in which $\underline{u} = \underline{0}$. To this purpose, matrix $\underline{\underline{\Delta}}$ is decomposed in its Jordan normal form: however, since matrices $\underline{\underline{M}}$ and $\underline{\underline{\Delta}}$ are related through Eq. (35), it can be shown that the following relationship holds true:

$$\underline{\underline{M}} = \underline{\underline{V}}_m\underline{\underline{J}}_m\underline{\underline{V}}_m^{-1} \quad \Leftrightarrow \quad \underline{\underline{\Delta}} = \underline{\underline{V}}_m\left(\frac{1}{T}\log\left(\underline{\underline{J}}_m\right)\right)\underline{\underline{V}}_m^{-1} = \underline{\underline{V}}_\lambda\underline{\underline{J}}_\lambda\underline{\underline{V}}_\lambda^{-1} \tag{38}$$

where the columns of matrices $\underline{\underline{V}}_\lambda$ and $\underline{\underline{V}}_m$ are the eigenvectors of matrices $\underline{\underline{\Delta}}$ and $\underline{\underline{M}}$, respectively, and matrices $\underline{\underline{J}}_\lambda$ and $\underline{\underline{J}}_m$ contain the eigenvalues of $\underline{\underline{\Delta}}$ and $\underline{\underline{M}}$ on their main diagonal. Each eigenvalue λ_i and associated eigenvector $\underline{v}_i$ of $\underline{\underline{\Delta}}$ allow defining a fundamental solution of the homogeneous equation of Eq. (37) in the form $\underline{\zeta}_i(t) = \underline{v}_i e^{\lambda_i(t-t_0)}$, representing a portion of the motion (i.e., a mode), which can be converted to a fundamental solution of the LTV system of Eq. (29) thanks to Eq. (36). By linearly combining the different fundamental solutions with a certain set of coefficients, represented by vector $\underline{c} = [c_1, c_2, \ldots, c_6]^T$, any solution can be described. If the fundamental solutions are grouped as the columns of a matrix $\underline{\underline{Z}}(t)$, then the general solution $\underline{x}(t)$ of Eq. (29) can be represented as follows:

$$\underline{x}(t) = \underline{\underline{\Psi}}(t)\underline{c} = \underline{\underline{P}}(t)\underline{\underline{Z}}(t)\underline{c} = \sum_{i=1}^{6} c_i\underline{\underline{P}}(t)\underline{v}_i e^{\lambda_i(t-t_0)} \tag{39}$$

If Eq. (39) is considered at the initial time $t = t_0$, then the relationship reported in Eq. (40) can be found relating the initial conditions $\underline{x}(t_0) = \underline{x}_0$ to the corresponding set of coefficients, or vice versa.

$$\underline{x}_0 = \underline{\underline{V}}_\lambda\,\underline{c} \tag{40}$$

All the terms in Eq. (39) can assume complex values: however, it is possible to retain an equivalent, fully real formulation of this equation if the fundamental solutions related to complex conjugate eigenvalues are refactored together. To this purpose, the following section recollects some common results that occur when analyzing LTV systems and, specifically, the relative dynamics in the CR3BP problem.

B. Common fundamental modal solutions and their refactorization

In a generic periodic LTV system, different solutions are observed depending on the nature of the eigenvalues of matrix $\underline{\mathbf{\Delta}}$. For example, a couple of conjugate imaginary eigenvalues corresponds to an oscillatory (center) mode; a purely real eigenvalue corresponds to a stable or unstable drifting mode depending on whether the eigenvalue is negative or positive; null eigenvalues correspond to trivial motions as defined in the following. Depending on the expected mode of motion, a different shape of the solution can be defined.

1. Trivial modes

As Burnett and Schaub highlight in Ref. [27], if the orbit of the target in the CR3BP problem is perfectly periodic then $\underline{\mathbf{\Delta}}$ has a null defective eigenvalue, having algebraic multiplicity of 2 (i.e., two eigenvalues λ_i and λ_j are identical and equal to 0) and geometric multiplicity of 1 (i.e., one linearly independent eigenvector is associated to it). Therefore, a generalized eigenvector $\underline{v}_j$ can be computed from $\underline{v}_i$ and a generic solution of Eq. (29) can be expressed as the sum of the two linearly independent solutions associated with the two eigenvectors $\underline{v}_i$ and $\underline{v}_j$, as shown in Eq. (41).

$$\underline{z}_{ij}(t) = c_i \underline{v}_i + c_j \left(\underline{v}_i (t - t_0) + \underline{v}_j \right) \tag{41}$$

The defective eigenvalue thus represents a trivial mode in which the motion is described by an offset term and a component drifting linearly with time. Notably, both eigenvectors are necessarily real since matrix $\underline{\mathbf{M}}$ and the two corresponding eigenvalues are real as well.

2. Stable and unstable modes

The modes associated with purely real eigenvalues of $\underline{\mathbf{\Delta}}$, i.e., stable and unstable modes, are also fully real in their description, since the corresponding eigenvectors must be real themselves. Therefore, given a real eigenvalue λ_i and the corresponding eigenvector $\underline{v}_i$, the stable or unstable mode is straightforwardly described by:

$$\underline{z}_i(t) = c_i \underline{v}_i e^{\lambda_i (t - t_0)} \tag{42}$$

3. Center modes

For what concerns the center modes, in the presence of two imaginary conjugate eigenvalues $\lambda_i = -i\omega_i$ and $\lambda_j = i\omega_i$ the conventional exponential solution can be rewritten as in Eq. (43) as a function of sine and cosine using Euler's formula.

$$\underline{z}_{ij}(t) = c_i \underline{v}_i \left[\cos(\omega_i(t - t_0)) + i \sin(\omega_i(t - t_0)) \right] + c_j \underline{v}_j \left[\cos(\omega_i(t - t_0)) - i \sin(\omega_i(t - t_0)) \right] \tag{43}$$

Following Refs. [26, 27], the two modes can be considered altogether to refactor them and remove the complex part. To this purpose, the two coefficients and eigenvalues are rewritten as a combination of a real part and an imaginary part as $c_{i,j} = c_R \pm i c_I$ and $\underline{v}_{i,j} = \underline{v}_R \pm i \underline{v}_I$ and are substituted in Eq. (43). By explicitly computing the products between coefficients, eigenvectors, and trigonometric functions, and then further manipulating Eq. (43), the following reformulation can be obtained which results in the two new, purely real fundamental solutions of the motion:

$$\underline{z}_{ij}(t) = c_R \left[2\underline{v}_R \cos(\omega_k(t - t_0)) - 2\underline{v}_I \sin(\omega_k(t - t_0)) \right] + \\ -c_I \left[2\underline{v}_R \sin(\omega_k(t - t_0)) + 2\underline{v}_I \cos(\omega_k(t - t_0)) \right] = c_R \underline{\zeta}_i(t) + c_I \underline{\zeta}_j(t) \tag{44}$$

If this refactorization is considered, the set of coefficients $\underline{c}$ and the matrix of eigenvectors $\underline{V}_\lambda$ must be modified to include coefficients c_R and c_I instead of c_i and c_j, and column vectors $2\underline{v}_R$ and $-2\underline{v}_I$ instead of $\underline{v}_i$ and $\underline{v}_j$ for Eq. (40) to still be valid. This assert is straightforwardly proven by evaluating Eq. (44) at the initial time t_0 and comparing it with Eq. (40).

4. Center modes approximating a trivial motion

Cases can occur in which the eigenvalues of the center modes feature a magnitude in the complex plane that is close to zero, as both the real and complex parts of the eigenvalue approach zero. In these cases, considering the general result $\underline{z}_i(t) = c_i \underline{v}_i e^{(\lambda_R + i\lambda_I)(t - t_0)}$, the LTI function can be approximated as $\underline{z}_i(t) \approx c_i \underline{v}_i$ if the exponent of the exponential is small, which occur over a time interval $t - t_0$ that becomes larger the smaller the magnitudes of λ_R and λ_I. Considering the two center modes simultaneously, a similar result to the one observed for the center modes is achieved using Eqs. (43) and (44), although the latter process also has the advantage of refactoring of the eigenvectors to remove their imaginary components. The latter approach can therefore be considered, observing that the resulting function $\underline{z}_{ij}$ is constant over time.

C. Geometrical analysis of the modes of motion

The refactorization of the solution presented in Eqs. (41)-(44) also highlights that the LTI equivalent of the solution of the LTV system obtained through modal decomposition can be characterized geometrically if the equations are further manipulated. Moreover, this geometric reformulation of the modal decomposition of the solution can also be carried on to the LTV equations. In fact, Eq. (39) clarifies that the LTV solution is a linear combination of the LTI solutions $\underline{z}_i = c_i \underline{\zeta}_i(t)$ according to the rows of matrix $\underline{P}(t)$, which change in magnitude and sign over time from the initial condition given by the identity matrix. This translates into the fact that the LTI solution provides a trend for the relative motion and matrix $\underline{P}(t)$ describes how the actual motion unfolds around such trend. Therefore, analyzing the LTI solution from a geometrical standpoint can provide a way of gaining further insight into the LTV one.

The analysis is conducted in this section by considering that the LTI state vector $\underline{z}$ is articulated as $\underline{z}(t) = [\underline{z}_p(t)^T, \underline{z}_v(t)^T]^T$. The reason for articulating $\underline{z}$ in these two subvectors is that, at time t_0 and after every period from t_0 going on, matrix $\underline{P}(t)$ equals identity and therefore $\underline{x} = \underline{z}$. In other words, for any integer k, vectors $\underline{z}_p(t_0 + kT)$ and $\underline{z}_v(t_0 + kT)$ directly represent the position and velocity of the LTV system: when computed at any other time instant t, the two subvectors $\underline{z}_p$ and $\underline{z}_v$ do not correspond to the position and velocity as described in the LTV state, but all contribute to each component of the LTV state as a result of the combination through the rows of $\underline{P}(t)$. The common types of modes previously discussed in Section III.B are now considered separately, focusing specifically on the stable/unstable and center modes. The trivial modes, in fact, have a directly interpretable geometrical meaning, as they represent an offset term with a linear drift in time.

In the case of stable and unstable modes, Eq. (42) can be easily rewritten accounting for the fact that the initial condition of the motion (i.e., $\underline{z}_i(t_0) = c_i \underline{v}_i e^{-\lambda_i t_0}$) scales the exponential term, resulting in the alternative formulation given by Eq. (45). Moreover, considering the equivalence of the LTI and LTV states at the initial condition, this also means that, for a stable or unstable mode, $\hat{z}_{i,v}(t_0)$ is the unit vector of the initial velocity of the motion, thus indicating the initial direction of evolution of the i-th mode. If the corresponding eigenvector $\underline{v}_i$ is articulated as $\underline{v} = [\underline{v}_{i,p}^T, \underline{v}_{i,v}^T]^T$ then $\hat{z}_{i,v}(t_0) = \hat{v}_{i,v}$, meaning that at t_0 the direction of evolution of the mode in the actual Cartesian state coincides with portion $\hat{v}_{i,v}$ of the corresponding eigenvalue.

$$\underline{z}_i(t) = c_i \underline{\alpha}_i e^{\lambda_i t}, \qquad \underline{\alpha}_i = \frac{\underline{v}_i}{e^{\lambda_i t_0}} \tag{45}$$

For what concerns the center modes, Eq. (44) shows that each refactored mode can be first rewritten as a vector of harmonic oscillators. Specifically, let us consider the generic couple i and j of center modes, for which the corresponding eigenvalues are $\lambda_i = -i\omega_i$ and $\lambda_j = +i\omega_i$, and let $z_{p,m}(t)$ be the m-th component of the p-th fundamental solution $\underline{z}_p(t)$, with $p = i, j$. The harmonic oscillators of the two modes assume the following form:

$$z_{i,m}(t) = \bar{A}_{i,m} \cos\left(\omega_i t - \phi_{0i} + \phi_{v_{ij}m}\right), \qquad z_{j,m}(t) = \bar{A}_{j,m} \sin\left(\omega_i t - \phi_{0i} + \phi_{v_{ij}m}\right),$$

$$\bar{A}_{p,m} = c_p \sqrt{v_{i,m}^2 + v_{j,m}^2} = c_p v_{ij,m}, \qquad p = i, j, \qquad \phi_{0i} = \omega_i t_0, \qquad \phi_{v_{ij}m} = \tan^{-1}\left(\frac{v_{j,m}}{v_{i,m}}\right) \tag{46}$$

Equation (46) highlights that, for each m-th component of the solution $\underline{z}_p(t)$, the amplitude $\bar{A}_{p,m}$ is a function of both the corresponding coefficient and the elements of the eigenvectors associated with the motion, while the phase $\phi_{v_{ij}m}$ is a function of the elements of the eigenvectors only. The motion $\underline{z}_{ij}(t)$ associated with the combination of the two harmonic oscillators is the sum of the two fundamental solutions associated with the center modes: however, since Eq. (46) highlights that the sine and cosine functions of the two modes share the same argument, it is therefore possible to condensate the center modes in a single oscillatory motion as per Eq. (47). The latter equation shows that any oscillatory motion in the LTI state-space is represented by a three-dimensional ellipse, which is described, both in

terms of its phase and amplitude, by the corresponding modal coefficients, which can therefore be interpreted as design variables.

$$z_{ij,m}(t) = \bar{A}_{ij,m} \sin\left(\omega_i t - \phi_{0i} + \phi_{v_{ij}m} + \phi_{c_{ij}}\right),$$

$$\bar{A}_{ij,m} = v_{ij,m}\sqrt{c_i^2 + c_j^2}, \qquad \phi_{c_{ij}} = \tan^{-1}\left(\bar{A}_{i,m}/\bar{A}_{j,m}\right) = \tan^{-1}\left(c_i/c_j\right) \tag{47}$$

The extension of these concepts to the LTV Cartesian state representation of the relative motion must consider the fact that the j-th component of the Cartesian state $\underline{x}$ results from a combination of all components of vector $\underline{z}$ according to the elements of the j-th row $\underline{p}_{r,j}(t)$ of matrix $\underline{P}(t)$. As such, it is a complicated time-varying combination of the terms of $\underline{z}$, which cannot be modelled analytically in the context of the CR3BP; nevertheless, useful relations can still be derived between the geometrical properties of the motion and the coefficients $\underline{c}$ if the single modes are analyzed separately and numerical analyses of the time-varying terms are performed. Notably, the latter depends on the absolute dynamics of the target: therefore, most analyses can be performed once and over a timespan that is limited to no more than a few orbit periods of the target. Starting with the case of the stable and unstable modes of the motion, the Cartesian relative state can be represented as follows for the generic i-th mode:

$$\underline{x}_i(t) = c_i \underline{p}_s(t) e^{\lambda_i t}, \qquad \underline{p}_s(t) = \left[\underline{p}_{r,1}^T(t)\underline{\alpha}_i, \dots, \underline{p}_{r,6}^T(t)\underline{\alpha}_i\right]^T \tag{48}$$

Equation (48) can be analyzed both component-wise and in terms of its norm. First, observing that each component of vector $\underline{z}_i$ in Eq. (45) is a monotone exponential function, the envelopes of the single components of the motion can be expressed as exponential functions multiplied by a constant coefficient given by the maximum or minimum of the dot product $\underline{p}_{r,j}^T(t)\underline{\alpha}_i$ over one orbit period of the target, as summarized in Eqs. (49) and (50) for the generic m-th component.

$$x_{inf,i,m}(t) = |c_i| m_{v_i,m} e^{\lambda_i t} \leq c_i \left(\underline{p}_{r,m}^T(t)\underline{\alpha}_i\right) e^{\lambda_i t}, \qquad m_{v_i,m} = \min_{t \in [t_0, t_0+T]} \left(\text{sign}(c_i)\underline{p}_{r,m}^T(t)\underline{\alpha}_i\right) \tag{49}$$

$$x_{sup,i,m}(t) = |c_i| M_{v_i,m} e^{\lambda_i t} \geq c_i \left(\underline{p}_{r,m}^T(t)\underline{\alpha}_i\right) e^{\lambda_i t}, \qquad M_{v_i,m} = \max_{t \in [t_0, t_0+T]} \left(\text{sign}(c_i)\underline{p}_{r,m}^T(t)\underline{\alpha}_i\right) \tag{50}$$

Consequently, the norm of the relative position vector ρ_i associated with the i-th mode has the same exponential trend of each component, which results in the actual evolution of the target-chaser distance once combined with matrix $\underline{P}(t)$. Therefore, the superior and inferior limiting functions are evaluated as in Eqs. (51) and (52), and describe the bounds of the approaching (departing) motion of a stable (unstable) mode, allowing an approach to (departure from) the target spacecraft that does not require additional control actions ideally. The choice of the coefficients to design the stable or unstable motion can be performed in different ways, such as by choosing the value that allows achieving a desired minimum target-chaser separation $\rho_{inf,i}(t_f)$ at a given final time t_f. As the sign of the coefficient does not affect the evolution of functions $\rho_{inf,i}(t)$ and $\rho_{sup,i}(t)$, it can be chosen depending on the direction of approach to the target by observing the sign of the elements of vector $\underline{v}_{i,p}$.

$$\rho_{inf,i}(t) = |c_i| d_{\rho,m} e^{\lambda_i t}, \qquad d_{\rho,m} = \min\left(\sqrt{m_{v_i,1}^2 + m_{v_i,2}^2 + m_{v_i,3}^2}, \sqrt{M_{v_i,1}^2 + M_{v_i,2}^2 + M_{v_i,3}^2}\right) \tag{51}$$

$$\rho_{sup,i}(t) = |c_i| d_{\rho,M} e^{\lambda_i t}, \qquad d_{\rho,M} = \max\left(\sqrt{m_{v_i,1}^2 + m_{v_i,2}^2 + m_{v_i,3}^2}, \sqrt{M_{v_i,1}^2 + M_{v_i,2}^2 + M_{v_i,3}^2}\right) \tag{52}$$

On the other hand, considering a generic couple of center modes i and j described in Eq. (47), it is possible to determine the expected maximum and minimum target-chaser separation during the corresponding quasi-periodic motion. To this purpose, each m-th component of the motion can be expressed as in Eq. (53) as the product of two vectors of periodic functions with different periods: specifically, the components of vector $\underline{p}_{r,m}(t)$ all have the same period T of the motion of the target on its orbit, while the components of vector $\underline{s}_{ij}(t)$ have period equal to $T_i = 2\pi/\omega_i$.

$$x_{ij,m}(t) = \left(\sqrt{c_i^2 + c_j^2}\right)\underline{p}_{r,m}^T(t)\underline{s}_{ij}(t), \qquad \underline{s}_{ij}(t) = \begin{bmatrix} v_{ij,1} \sin\left(\omega_i t - \phi_{0i} + \phi_{v_{ij}m} + \phi_{c_{ij}}\right) \\ \vdots \\ v_{ij,6} \sin\left(\omega_i t - \phi_{0i} + \phi_{v_{ij}m} + \phi_{c_{ij}}\right) \end{bmatrix} \tag{53}$$

Periods T and T_i are usually incommensurable and the norm $\rho_{ij}(t)$ of the relative position vector behaves like a quasi-periodic function. Searching for the superior and inferior limits of the motion thus requires numerically computing the maximum and minimum values of $\rho_{ij}(t)$ as per Eq. (54), where T_f is the smallest temporal interval over which the maximum and minimum shall be computed. The latter is taken as the closest larger integer multiple of period T_i, evaluated as if T and T_i were commensurable; in this way, approximations of the superior and inferior limits can be computed easily while considering the quasi-periodicity of the motion.

$$
\begin{aligned}
\rho_{inf,ij} &= \min_{t \in [t_0, t_0+T_f]} \rho_{ij}(t) \\
\rho_{sup,ij} &= \max_{t \in [t_0, t_0+T_f]} \rho_{ij}(t)'
\end{aligned}
\qquad \rho_{ij}(t) = \sqrt{x_{ij,1}^2(t) + x_{ij,2}^2(t) + x_{ij,3}^2(t)}, \qquad T_f = \mathrm{ceil}\left(\frac{T_i}{T}\right) T_i
\tag{54}
$$

The quasi-periodic motion resulting from the activation of a center mode can thus be designed observing that, if a spherical keep-out zone of radius r_{KOZ} is considered, the latter can be related to the coefficients of modal decomposition as per Eq. (55), which results from the manipulation of Eq. (54) and imposing that $\rho_{inf,ij} = r_{KOZ}$. From a general standpoint, this equation would require an iterative resolution of the problem due to m_{ij} being dependent on coefficients c_i and c_j. Moreover, the equation only provides one constraint, thus leaving space for a second constraint to be applied to fix the value of the other coefficient. In this respect, if c_i is set to zero as an additional constraint, then the term $\phi_{c_{ij}}$ in the elements of vector $\underline{s}_{ij}(t)$ of Eq. (53) can be nullified. In doing so, the coefficient m_{ij} of Eq. (55) becomes constant for different values of c_j, and Eq. (55) can be inverted to find the value of c_j that ensures that $\rho_{ij}(t)$ never falls below r_{KOZ}. The same can be done if c_j is set to zero, which instead results in $\phi_{c_{ij}} = \pi/2$.

$$
r_{KOZ} = \sqrt{c_i^2 + c_j^2}\, m_{ij}(c_i, c_j),
$$
$$
m_{ij}(c_i, c_j) = \min_{t \in [t_0, t_o+T_f]} \sqrt{\left(\underline{p}_{r,1}^T \underline{s}_{ij}(t)\right)^2 + \left(\underline{p}_{r,2}^T(t)\underline{s}_{ij}(t)\right)^2 + \left(\underline{p}_{r,3}^T(t)\underline{s}_{ij}(t)\right)^2}
\tag{55}
$$

Notably, the resulting quasi-periodic motion is bounded, and therefore a maximum target-chaser separation can also be identified as the radius r_{KIZ} of a spherical keep-in zone, which can be computed as per Eq. (56), obtained by manipulating Eq. (54) and imposing that $\rho_{sup,ij} = r_{KIZ}$. The same observations reserved to Eq. (55) apply to Eq. (56) as well, and the latter may also be employed for relative motion design, although it may be less desirable compared to a condition on the minimum target-chaser separation as the one provided in Eq. (55).

$$
r_{KIZ} = \sqrt{c_i^2 + c_j^2}\, M_{ij}(c_i, c_j),
$$
$$
M_{ij}(c_i, c_j) = \max_{t \in [t_0, t_o+T_f]} \sqrt{\left(\underline{p}_{r,1}^T \underline{s}_{ij}(t)\right)^2 + \left(\underline{p}_{r,2}^T(t)\underline{s}_{ij}(t)\right)^2 + \left(\underline{p}_{r,3}^T(t)\underline{s}_{ij}(t)\right)^2}
\tag{56}
$$

In the case of a center mode approximating a trivial motion as considered in Section III.B.4, function $\underline{s}_{ij}$ of Eq. (53) is approximated with a constant vector since $\omega_i \approx 0$. As a result, the motion is once again periodic with period T and the maximum and minimum values of the relative distance $\rho_{ij}(t)$ can be computed as per Eqs. (54)-(56) but over a single period T of the orbit of the target spacecraft. Therefore, the same considerations related to the design of a quasi-periodic motion using the center modes can be applied in this case as well.

IV. Results

The assessment of the accuracy with which the model obtained through the fundamental modal solutions method represents the relative motion and its employment for guidance and path-planning purposes are investigated in this Section. Specifically, the non-linear and linearized relative motion equations derived in Section II.B are first tested to verify the accuracy with which they can model the relative dynamics. To this purpose, the motion is propagated from an arbitrarily chosen initial condition using both the linear and non-linear equations of relative motion, and these are compared with the relative state computed by numerically propagating the target and chaser orbits separately in the CR3BP. Errors on the state variables between the different models are computed according to Eq. (57), where subscript "r" identifies the reference solution. The error components are all computed between quantities expressed and

observed in the VRF. To conduct a thorough comparison, first, the linearized solution is compared against the non-linear one taken as a reference, to assess the effect of linearization; then, a comparison is made between the linearized and non-linear equations of motions against the reference solution obtained by numerically propagating the CR3BP equation. Subsequently, the modal decomposition approach presented in Section III is applied to the relative dynamics equations in the velocity frame; given the periodicity of matrix $\underline{P}(t)$, the latter will be evaluated over a period and interpolated to be used over multiple periods, so that the burden of computing matrix $\underline{P}(t)$ at every instant is removed from the model. However, it must be noted that this is a simplifying assumption that might introduce errors if the system under consideration is not exactly periodic. The accuracy with which the modal decomposition model can be used to propagate the relative motion is then assessed in the same way as the linearized and non-linear equations of relative motion, with an additional comparison between the modal solution and the linearized one taken as a reference.

$$
\begin{aligned}
e_x &= x - x_r, & e_{\dot{x}} &= \dot{x} - \dot{x}_r \\
e_y &= y - y_r, & e_{\dot{y}} &= \dot{y} - \dot{y}_r \\
e_z &= z - z_r, & e_{\dot{z}} &= \dot{z} - \dot{z}_r
\end{aligned}
\tag{57}
$$

The set of modal solutions computed in this way is then used first to analyze the fundamental components of the relative motion in the velocity frame and characterize them from a geometrical standpoint, and later to compute target conditions for a path-planning strategy for CPOs to approach a target object. In this context, a state-of-the-art method is employed to compute fuel-efficient impulsive approach maneuvers, adapted to use the coefficients of modal decomposition as ROEs. To verify that the maneuvers effectively allow reaching the desired target state, the difference between the achieved and desired ROEs is observed, while the overall cost of the maneuvers is evaluated by summing the norms of the ΔV vectors describing each impulsive burn.

The analyses presented in this Section are conducted considering a study case in which the target spacecraft is located on a nearly stable halo orbit around the L2 point, the initial conditions of which are reported in dimensionless Cartesian coordinates in Table 1. The gravitational parameters ratio for the Earth-Moon system is taken as $\mu = 1.215 \times 10^{-2}$ and the reference quantities considered to retrieve dimensional quantities from the dimensionless ones are summarized in Table 2. The initial condition of the target, the reference dimensional quantities, and parameter μ are all retrieved from the NASA Jet Propulsion Laboratory Three-Body Periodic Orbit Catalog[*].

Table 1 Dimensionless initial conditions of the L2 halo orbit of the target spacecraft, expressed in both the classical synodal barycentric frame and the MRF frame.

Frame	Components of initial state vector, $\underline{r}$					
	X	Y	Z	$\dot{X}$	$\dot{Y}$	$\dot{Z}$
Synodal	1.08296	0	2.02317	0	–2.01026	0
MRF	–0.095106	0	0.202317	0	0.201026	

Table 2 Reference dimensional quantities.

Reference quantity	r_{em}	ω_{mi}
Value	3.89703×10^8 m	2.61110×10^{-6} rad/s

A. Application of modal decomposition to the velocity frame

In order to apply the methodology discussed in Section III, Eq. (29) is first numerically integrated together with the equations of the absolute motion (3) and the fundamental matrix equation (31) over a full target orbit period T, representing the angular velocity and acceleration terms as per Eqs. (9), (10), (24), and (25) and jerk term as per Eq. (27). The STM resulting from the final step of the numerical integration is the monodromy matrix $\underline{M}$ of the system, from which matrix $\underline{\Lambda}$ and the corresponding eigenvalues and eigenvectors can be computed as per Eqs. (35) and (38). The resulting eigenvalues are represented in Fig. 2.a, showing that, in the considered system and for initial conditions of the target spacecraft given in Table 1, there exist one stable and one unstable modes and four center modes;

---

specifically, the center modes all have null real part, and two of them feature a very small imaginary part (in the order of 10^{-5}). The presence of this pair of imaginary conjugate eigenvalues that are very close to zero can be related to the fact that the selected L2 orbit is not perfectly periodic. However, while the magnitude of the imaginary part may be considered almost negligible, the corresponding modes cannot be directly treated as a trivial pair without introducing an error in the representation that increases over time: therefore, this couple of modes must be treated as a couple of center modes. Applying the refactorization suggested in Section III.B, the following representation of the fundamental solutions can be considered, in which a change in nomenclature is applied to make the notation more concise:

$$\underline{z}_1(t) = c_1 \underline{v}_1 e^{\lambda_1(t-t_0)}, \quad \lambda_1 \in R, \quad \lambda_1 > 0$$
$$\underline{z}_2(t) = c_2 \left[\underline{v}_2 \cos(\omega_2(t-t_0)) - \underline{v}_3 \sin(\omega_2(t-t_0)) \right]$$
$$\underline{z}_3(t) = c_3 \left[\underline{v}_2 \sin(\omega_2(t-t_0)) + \underline{v}_3 \cos(\omega_2(t-t_0)) \right]$$
$$\underline{z}_4(t) = c_4 \left[\underline{v}_4 \cos(\omega_4(t-t_0)) - \underline{v}_5 \sin(\omega_4(t-t_0)) \right]$$
$$\underline{z}_5(t) = c_5 \left[\underline{v}_4 \sin(\omega_4(t-t_0)) + \underline{v}_5 \cos(\omega_4(t-t_0)) \right] \tag{58}$$
$$\underline{z}_6(t) = c_6 \underline{v}_6 e^{\lambda_6(t-t_0)}, \quad \lambda_6 \in R, \quad \lambda_6 < 0$$
$$\omega_2 = |\text{imag}(\lambda_2)| = |\text{imag}(\lambda_3)|, \qquad \omega_4 = |\text{imag}(\lambda_4)| = |\text{imag}(\lambda_5)|$$
$$\underline{c} = [c_1, \; c_2, \; c_3, \; c_4, \; c_5, \; c_6]^T = [c_1, \; c_{R1}, \; c_{I1}, \; c_{R2}, \; c_{I2}, \; c_6]^T$$
$$\underline{V} = \left[\underline{v}_1, \; \underline{v}_2, \; \underline{v}_3, \; \underline{v}_4, \; \underline{v}_5, \; \underline{v}_6 \right] = \left[\underline{v}_1, \; 2\underline{v}_{R1}, \; -2\underline{v}_{I1}, \; 2\underline{v}_{R2}, \; -2\underline{v}_{I2}, \; \underline{v}_6 \right]$$

For completeness, Fig. 2.b also shows the eigenvectors associated with matrix $\underline{\Delta}$ as already refactored according to Eq. (58). At a first glance, it is evident that the refactorization drastically reduces the magnitude of $\underline{v}_5$, that is not visible in this plot and whose components are of the same order of magnitude of the corresponding eigenvalue. In fact, coherently with λ_4 and λ_5 being close to zero, their eigenvectors are similar and thus their combination during refactorization results in $\underline{v}_5$ having second, fourth, and sixth components close to zero ($\approx 10^{-15}$), and the first, third, and fifth components equal to -5.228×10^{-6}, -1.229×10^{-5}, and -1.103×10^{-6}. Eigenvector $\underline{v}_4$, on the other hand, has its second component to be the largest of the set, while all other components are negligible ($\approx 10^{-10}$). This has an important geometrical meaning: in fact, since ω_4 is in the order of 10^{-5}, the period of the oscillations described in $\underline{z}_4(t)$ and $\underline{z}_5(t)$ in Eq. (58) is in the order of 10^5. This implies that over the typical interval of interest of the propagation, the term resulting from $\underline{z}_4(t) + \underline{z}_5(t)$ takes the form of an offset along the velocity axis summed with a linear drift trend superimposed to an oscillation having the same period as the target orbit; modes 4 and 5 thus represent a center mode approximating a trivial motion. This is coherent with the fact that if the chaser is on the same orbit of the target (i.e., only the fourth coefficient of the set is non-zero), at the initial time the two spacecraft will only be separated in the velocity direction and the chaser will oscillate along this direction as time passes. In the case of the modal decomposition, this oscillatory part is provided by the LF transformation matrix. If a positive fifth coefficient is considered, this results in an initial condition having a vertical component that is smaller, due to the first component of vector $\underline{v}_5$, which can be interpreted similarly to a reduction of the semimajor axis in an orbit around the Earth, resulting in a drift along the negative flight-path direction, as the negative sign of the fifth component of $\underline{v}_5$ shows. Once again, this term combines with the periodic oscillation given by matrix $\underline{P}(t)$.

a) Eigenvalues in the complex plane, with unit circle in black. In the red box inset: zoom on eigenvalues λ_4 and λ_5.
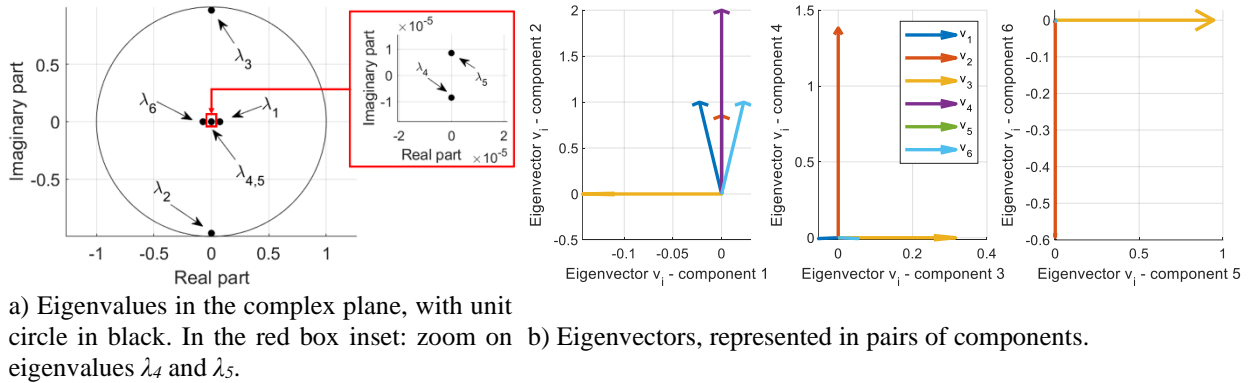
b) Eigenvectors, represented in pairs of components.

Fig. 2 Representation of eigenvectors and eigenvalues of the state matrix $\underline{\Delta}$ of the equivalent LTI system.

Finally, it is worth noting that the eigenvectors $\underline{v}_2$ and $\underline{v}_3$, associated with the primary center mode, have non-zero components placed in complementary locations: in other words, while $\underline{v}_2$ has second, fourth and sixth non-zero components, $\underline{v}_3$ has the first, third and fifth components as the non-zero ones.

A representation of the evolution of the relative motion from the arbitrary initial condition given by coefficients vector $\underline{c} = [5 \times 10^{-7}, 2 \times 10^{-6}, 2 \times 10^{-6}, 5 \times 10^{-7}, 1 \times 10^{-7}, 5 \times 10^{-7}]$ as propagated through Eq. (39) is shown in Fig. 3.a and Fig. 3.b compared to the direct integration of both the non-linear and linear equations of relative motion given by Eqs. (28) and (29), respectively, and to the relative motion of the chaser with respect to the target obtained by integrating the CR3BP equations for the two spacecraft. In this respect, Fig. 4.a reports the component-wise errors that the modal decomposition model shows when compared with the linear equations of motion. As expected, the two sets of propagated states are in good accordance with one another, the modal decomposition being derived from the latter using the mathematical instruments introduced in Section III. The errors between the modal and linear representation compared against the non-linear model are instead reported in Fig. 4.b: the graph shows that errors are at least two orders of magnitudes smaller than the magnitude of the relative state, confirming that, in the considered conditions, the linearized model of the relative motion can represent the motion with enough accuracy to be a valuable substitute for the non-linear equations of motion.

a) Three-dimensional view of the relative motion. b) Components of the Cartesian state vector.
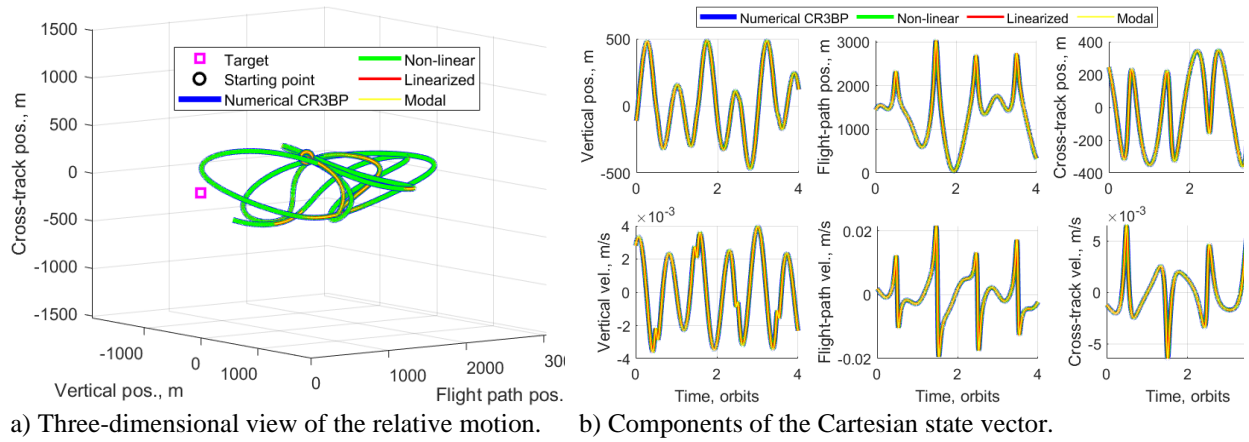
Fig. 3 Propagation of relative motion through modal decomposition model and comparison with the linearized and non-linear models of relative motion and the numerical integration of the CR3BP equations.

More interesting results stem from observation of Fig. 4.c, depicting the errors of the modal, linear and non-linear models compared with the numerically integrated motion in CR3BP. First, the graphs show that, as expected, there is a negligible error (in the order of 10^{-5} m in position and 10^{-9} m/s in velocity) between the representation of the state given by the non-linear equations and the relative state obtained by direct integration of the CR3BP equations. The reason is that the non-linear dynamics constitute a direct representation of the relative motion as it would be observed in the VRF. As a result, the comparison between the modal and linear solutions against the numerical integration of the CR3BP equations shows the same trend that is observed in Fig. 4.b. As a last remark, it is worth noting that both in Fig. 4.b and Fig. 4.c the error increases in magnitude over time but featuring an oscillatory trend. This is a linearization error, and its trend is associated with the fact that the system is not perfectly periodic as the eigenvalues reported in Fig. 2.a highlight. The result of this analysis thus shows that the considered linearized model, and equivalently its modal decomposition representation, can be used to describe the relative motion with an accuracy at least two orders of magnitude smaller than the relative state itself for multiple orbit periods. To retain such accuracy over time, the linearization requires to be periodically recomputed.
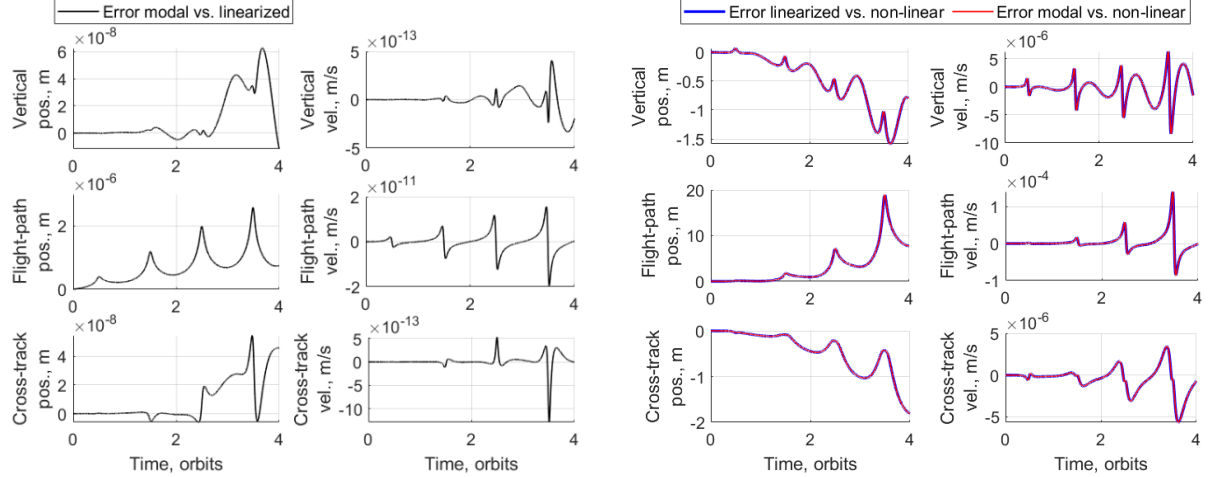
a) Errors of modal decomposition model compared against the linearized model.

b) Errors of modal decomposition and linearized models compared against the non-linear model.
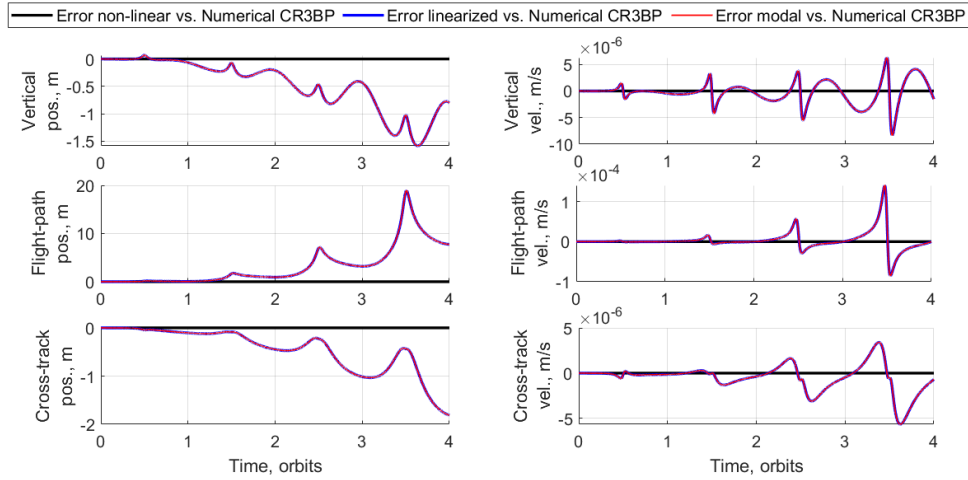
c) Errors of modal decomposition, linearized, and non-linear models against the numerical integration of the CR3BP equations.

Fig. 4 Errors on the components of the Cartesian representation of the propagated relative state.

In addition, Fig. 5 shows the three-dimensional evolution of the single modes of the motion. First of all, the drifting modes 1 and 6 in Fig. 5.a evidently represent such behavior but simultaneously show an initial offset with respect to the flight-path axis, as well as an oscillatory component along all directions, the largest and most evident one being in the flight-path direction. This component is periodic with period T and while its oscillatory behavior is due to matrix $\underline{P}(t)$, the direction of oscillation is related to the non-zero terms of eigenvectors 1 and 6: Fig. 2.b shows, in fact, that components 1 to 3 of both $\underline{v}_1$ and $\underline{v}_6$ are all non-zero, although the second one is the largest. Mode 2 and 3, shown in Fig. 5.b, coherently represent an oscillation around the target but feature a quasi-periodic motion. The quasi-periodicity is due to the incommensurability between the LTI description of the solution, periodic with period $2\pi/\omega_2$, and the LF matrix $\underline{P}(t)$, periodic with period $T = 2\pi/\omega_{mi}$. Lastly, Fig. 5.c highlights that mode 5 shows the smallest contribution to the motion and mode 4 translates into a bounded periodic motion. This oscillation is specifically the effect of matrix $\underline{P}(t)$ over the constant offset that mode 4 represents in the LTI state-space.

The same motion represented in Fig. 3.a and Fig. 3.b is shown in the LTI state-space in Fig. 6. Comparing this representation with the one in the LTV state-space of Fig. 3 and recalling that the LTI solution is represented by the modal decomposition of Eq. (58), this confirms that the LTI representation equivalent to the LTV system provides a more intuitive description of the relative motion. In fact, the complexity of the motion represented in Fig. 3.a and Fig. 3.b is due to the temporal evolution of the LF transformation matrix $\underline{P}(t)$.
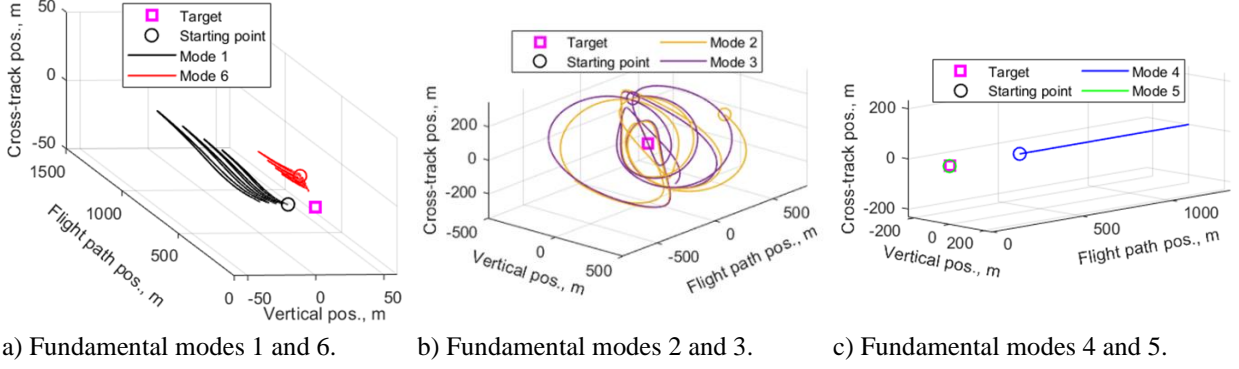
a) Fundamental modes 1 and 6. b) Fundamental modes 2 and 3. c) Fundamental modes 4 and 5.

Fig. 5 Three-dimensional Cartesian representation of the fundamental modes of the motion shown in Fig. 3, according to Eq. (58).

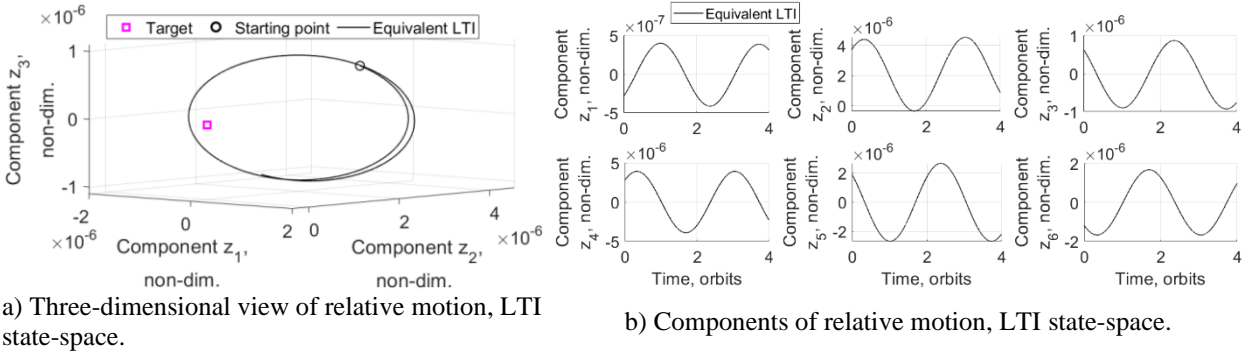a) Three-dimensional view of relative motion, LTI state-space.

b) Components of relative motion, LTI state-space.

Fig. 6 Equivalent representation in the LTI state-space of the relative motion shown in Fig. 3.

B. Geometrical characterization of the relative motion

The modal decomposition of the relative motion obtained in the previous Section IV.A is here applied to the design of simple motions using the coefficients of the decomposition as ROEs. A case is considered for each characteristic motion according to the geometrical interpretations given in Section III.B to highlight how each geometrical parameter can be used in conjunction with the coefficients for relative motion design. In the following, each motion is propagated by both using the modal decomposition model and numerically integrating the CR3BP equations of the absolute dynamics of the target and chaser spacecraft.

1. Drifting motion towards the target

The following case exemplifies the use of the coefficients of the stable mode to design a natural drifting motion that occurs approximately along the flight-path axis and allows approaching the target object from the negative flight-path direction, such that the arrival point is at a separation $\bar{\rho}_{des}$ from the target of 20 m. Considering the periodicity of the motion on the stable manifold, the target condition can be achieved safely on one of the local minima of the target-chaser separation function $\rho_i(t)$. Therefore, based on Eq. (51) and imposing $\rho_{inf,i}(t_f) = \rho_{des}$, the condition provided in Eq. (59) can first be applied to ensure that the coefficient c_6 is chosen so that the closest point of the drifting motion is at a distance $\rho_{des} = \bar{\rho}_{des}/r_{em}$ from the target. Then, Eq. (60) can be solved numerically to find the value of t_f that simultaneously satisfies Eqs. (59) and (60). The sign of the coefficient is finally chosen to be negative observing the eigenvector of the mode. This design problem is solved considering initial conditions to be computed at $t_0 = 0.5\ T$, i.e., the target initial state on the L2 orbit is considered as propagated from the conditions in Table 1 for half an orbit period. Considering the periodicity of the motion on the stable manifold, these conditions allow placing the target directly on the portion of the relative trajectory of the stable mode that moves towards the target.

$$|c_i(t_f)| = \rho_{des}/(d_{\rho,m}e^{\lambda_i t_f}) \tag{59}$$

$$\rho_i(t_f) = |c_i(t_f)| \left(\sqrt{\left(\underline{\boldsymbol{p}}_{r,1}^T(t_f)\underline{\boldsymbol{\alpha}}\right)^2 + \left(\underline{\boldsymbol{p}}_{r,2}^T(t_f)\underline{\boldsymbol{\alpha}}\right)^2 + \left(\underline{\boldsymbol{p}}_{r,3}^T(t_f)\underline{\boldsymbol{\alpha}}\right)^2} \right) e^{\lambda_i t_f} \qquad (60)$$

The solution of Eqs. (59) and (60) results in $t_f = 0.979\ T$, i.e., 10.34 days, which is coherently close to a full period of the orbit, where the next minimum of the function $\rho_i(t)$ is expected, and $c_6 = -1.9566 \times 10^{-7}$ with all other coefficients equal to zero. The motion is represented in Fig. 7.a in terms of the Cartesian components of the motion, also including the inferior and superior limits for each component computed as per Eqs. (49) and (50), while Fig. 7.b shows the evolution of the target-chaser separation together with the inferior and superior limits $\rho_{inf,i}(t)$ and $\rho_{sup,i}(t)$, computed as per Eqs. (51) and (52). The chaser successfully coasts towards the desired condition along an approach direction that is almost parallel to the flight-path axis, differing from the latter due to the properties of the stable manifold.
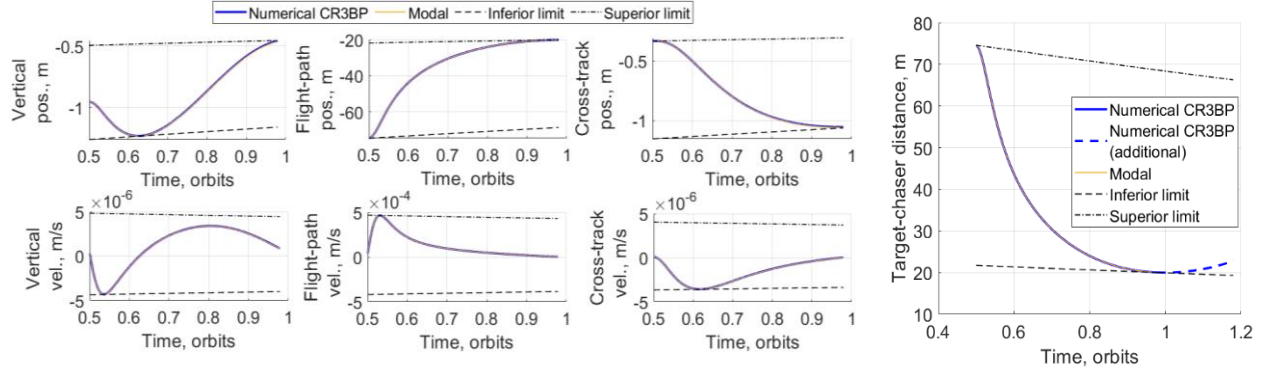
a) Cartesian components of the relative motion, with inferior and superior limits for each component.

b) Target-chaser separation, with superior and inferior limits.

Fig. 7 Natural drifting motion towards the target, obtained by activating the stable mode of the relative motion.

As a last remark, the minimum desired separation of 20 m is not overcome during the approach, as shown by Fig. 7.b, where the motion is propagated for a further 0.2 orbits to show that the constraint is satisfied. Overall, Fig. 7 highlights the good agreement between the modal decomposition approach and the motion propagated using the CR3BP equations, as well as between the models of the geometrical properties described in Eqs. (49)- (52) and the actual motion. Specifically, the largest error between the modal decomposition representation and the numerical integration of the CR3BP equations is expectedly obtained at the end of the propagation, with mm-level error on the relative position and errors in the order of 10^{-8} m/s on the norm of the relative velocity vector. A similar approach to the one considered in this section can also be considered when dealing with the design of a drifting motion departing from the target spacecraft using the unstable mode.

2. Quasi-periodic motion around the target
The second case under consideration uses the center modes of the motion to design a quasi-periodic trajectory around the target that must not violate a keep-out sphere of radius $\overline{r}_{KOZ} = 30$ m. As no specific constraint is imposed on the initial conditions of the motion, the design can be conducted by imposing $c_2 = 0$ and computing c_3 according to Eq. (55), considering the dimensionless quantity $r_{KOZ} = \overline{r}_{KOZ}/r_{em}$. For $t_0 = 0$, coefficient c_3 is set to 5.3257×10^{-7} and all other coefficients are considered to be zero. The sign of the coefficient affects the initial condition of the motion: as no specific constraint is considered in this respect, the coefficient is taken positive for simplicity and without loss of generality. The resulting motion is shown in three dimensions in Fig. 8.a, which highlights that the designed trajectory effectively stays out of the desired spherical keep-out zone. This is more evident observing the temporal evolution of the target-chaser separation reported in Fig. 8.b, where the superior and inferior limits are computed according to Eqs. (55) and (56), which also highlights the accuracy of the proposed modeling of the minimum and maximum target-chaser separation. Propagating the motion further in time, slight violations of the superior and inferior limits on the target-chaser distance may occur which are related to the approximated T_f considered in Eq. (54); however, these can be easily dealt with by applying a safety margin on the required r_{KOZ}. Moreover, Fig. 8.b and Fig. 8.c further highlight the accordance between the motions propagated using the modal decomposition model and the

19

CR3BP equation. Specifically, the maximum errors between the modal decomposition representation and the numerical integration of the CR3BP equations are coherently achieved at the end of the propagation and are in the orders of the centimeters for the relative position and of 10^{-8} m/s for the relative velocity.
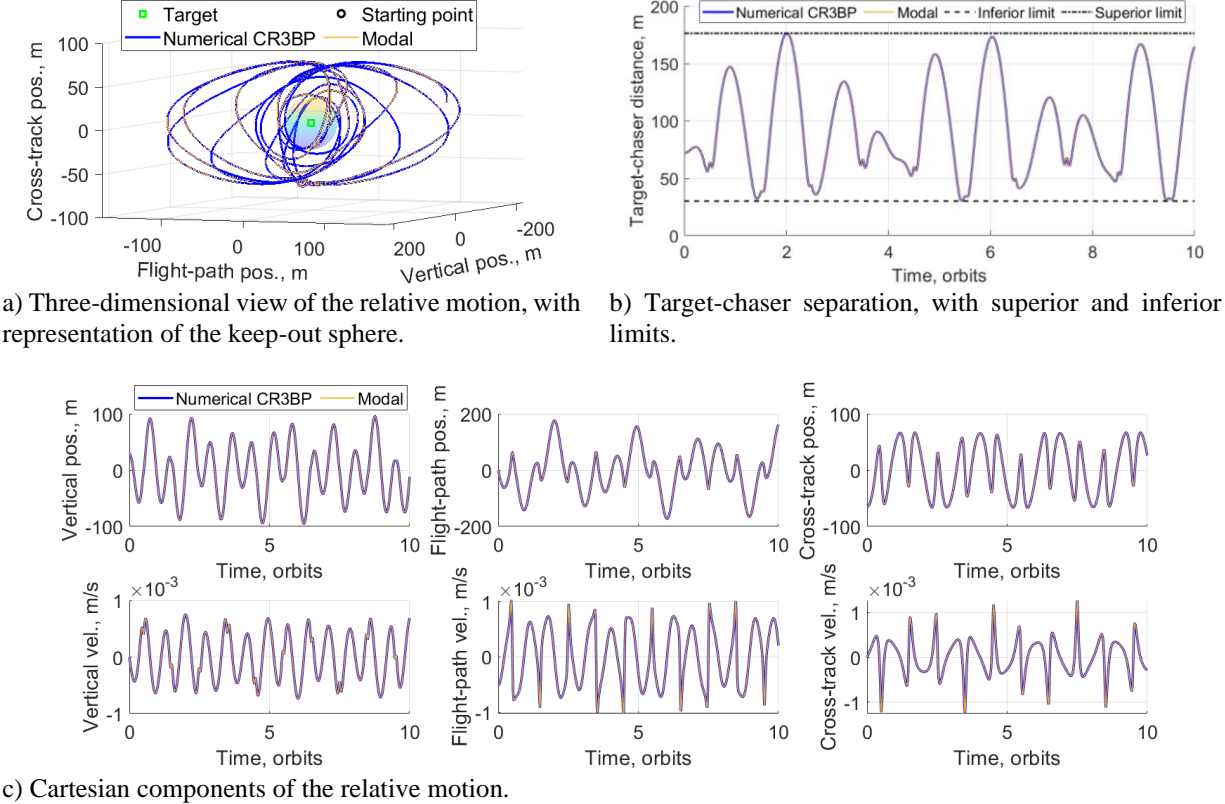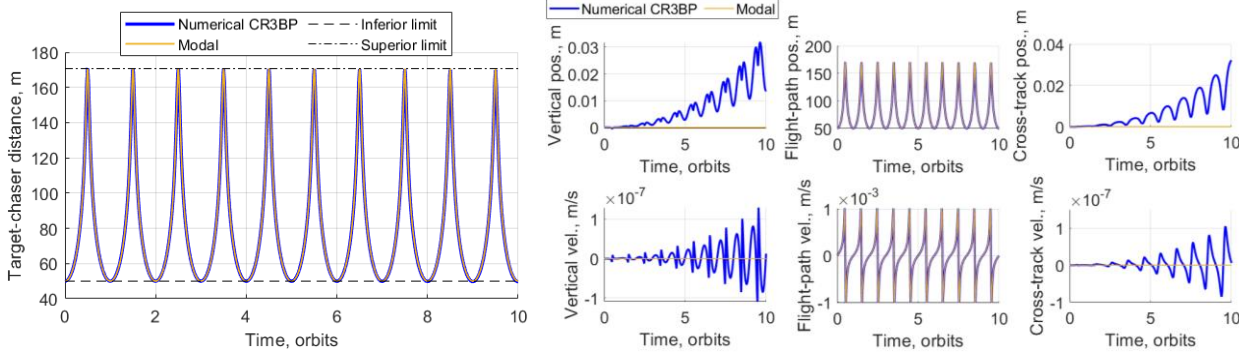

a) Three-dimensional view of the relative motion, with representation of the keep-out sphere.

b) Target-chaser separation, with superior and inferior limits.

c) Cartesian components of the relative motion.

Fig. 8 Quasi-periodic motion around the target spacecraft, designed to not violate a keep-out sphere of 30 m around the target spacecraft.

3. Bounded motion along the flight-path direction

A final design case is considered in which the chaser spacecraft is required to perform a bounded motion along the flight-path direction with a minimum target-chaser separation $\bar{r}_{KOZ}$ of 50 m. Such a bounded motion is desirable, for example, when the chaser is required to wait in between two approach sequences without drifting away from the target object. While a specific relative position in the Cartesian state-space can be maintained with respect to the target by using a continuous control profile, a natural motion that satisfies the desired property can be achieved by activating the center modes approximating the trivial motion. In this case, by observing that $\underline{v}_4$ has only the second component being substantially different from zero at $t_0 = 0$, while all components of $\underline{v}_5$ approach zero (see Fig. 2.b), then $c_5 = 0$ can be imposed and Eq. (55) be used once again to compute the desired value of c_4, considering $r_{KOZ} = \bar{r}_{KOZ}/r_{em}$. This results in $c_4 = 6.4151 \times 10^{-8}$ and all other coefficients can be set to zero; as for the choice on the sign of the coefficient, eigenvalue $\underline{v}_4$ shows that a positive coefficient allows placing the chaser in a leading position with respect to the target. The propagated motion is shown in Fig. 9 in terms of the target-chaser separation and of the single components of the Cartesian state vector; specifically Fig. 9.a shows that the motion is effectively bounded and always stays above the desired target-chaser separation. As in the previous case, the superior and inferior limits of the motion are computed using Eqs. (55) and (56). While the modal propagation of the motion is expectedly contained within the prescribed bounds at any time, the numerical propagation of the motion through the CR3BP equations begins to slightly violate the boundaries after 10 orbital periods (i.e., 105.65 days). This is due to the error build-up of the modal decomposition propagation, which is evident from Fig. 9.b and amounts to a few centimeters and to less than hundredths of mm/s after 10 orbits.

a) Target-chaser separation, with superior and inferior limits.

b) Cartesian components of the relative motion.

Fig. 9 Bounded motion with respect to the target, occurring along the flight-path direction and designed to not violate a minimum target-chaser separation of 50 m.

C. Modal coefficients as relative orbital elements for path-planning

The final contribution of this work investigates the use of the coefficients of modal decomposition as ROEs for the design of fuel-optimal approach trajectories. As for other sets of ROEs, the coefficients of modal decomposition allow computing transfers directly in the ROEs state-space, thus designing the approach trajectory as a series of maneuvers that allow the chaser to transfer between different relative trajectories, each represented by a set of coefficients. To this purpose, impulsive control actions are evaluated by applying a method originally proposed by Guffanti and D'Amico [30] and reformulated to consider the coefficients of modal decomposition as ROEs. Considering a predetermined duration of the transfer, the method computes the optimal times of applications of the impulsive control actions and the corresponding ΔVs, breaking down the transfer to pass through multiple intermediate states if required. The result is an approach trajectory composed of several connected segments on which the chaser can coast freely and apply impulsive ΔV when required. Notably, this approach provides a desirable control over the relative states through which the chaser shall transfer to perform the approach, which can be selected to satisfy some desired constraints (e.g., safety or operational constraints involving minimum target-chaser separations).

As the approach occurs, the accuracy with which a desired state is achieved is evaluated by comparing the achieved and desired set of coefficients $\hat{\underline{c}}_i$ and $\underline{c}_i$. The evaluation is also assisted by the observation of the Cartesian representation of the relative state. Finally, the cost of the approach is evaluated by observing the ΔV required for each transfer.

1. Impulsive burns computation method

In their work, Guffanti and D'Amico [30] highlight that, in general, a relative motion can be decomposed in an osculating term $\underline{F}'(\underline{x}, t)$, a perturbing term $\underline{F}_p(\underline{x}, t)$, and a control term, according to Eq. (61). Defining $\underline{\kappa}$ a set of constants of integration of this motion and considering that the osculating motion $\partial\underline{x}/\partial t = \underline{F}'(\underline{x}, t)$ corresponds to a single set $\underline{\kappa}$, the relative dynamics of Eq. (61) can equivalently be represented using the integration constants variational equation reported in Eq. (62), where $[\partial\underline{\kappa}/\partial\underline{x}]$ is the Jacobian matrix of the mapping function between the constants of integration $\underline{\kappa}$ and the Cartesian relative state $\underline{x}$.

$$\dot{\underline{x}}(t) = \underline{F}'(\underline{x}, t) + \underline{F}_p(\underline{x}, t) + \underline{\underline{B}}(t)\underline{u}(t) = \frac{\partial\underline{x}(\underline{\kappa}, t)}{\partial t} + \left[\frac{\partial\underline{x}(\underline{\kappa}, t)}{\partial\underline{\kappa}}\right]\frac{\partial\underline{\kappa}}{\partial t} + \underline{\underline{B}}(t)\underline{u}(t) \tag{61}$$

$$\dot{\underline{\kappa}} = \left[\frac{\partial\underline{\kappa}}{\partial\underline{x}(\underline{\kappa}, t)}\right]\underline{F}_p(\underline{x}, t) + \left[\frac{\partial\underline{\kappa}}{\partial\underline{x}(\underline{\kappa}, t)}\right]\underline{\underline{B}}(t)\underline{u}(t) \tag{62}$$

Reformulating Eq. (62) using the coefficients of the modal decomposition as constants of integration, being $\underline{c}$ a set of constants of the motion, Eq. (33) results in $[\partial\underline{c}/\partial\underline{x}] = \underline{\underline{\Psi}}^{-1}(t)$. As for the perturbing term, in the following it is neglected without loss of generality as no perturbing actions are included. At this point, the formulation proposed in

21

Ref. [30] can be employed to solve the optimization problem reported in Eq. (63) to obtain the directions of the optimal impulsive burns $\Delta \hat{v}(t_i) = \underline{\underline{B}}_c{}^T(t_i)\underline{\eta}$ as those that satisfy the condition $\| \underline{\underline{B}}_c{}^T(t_i)\underline{\eta} \| = 1$ at the times t_i, for $\underline{\underline{B}}_c(t_i) = \underline{\underline{\Psi}}^{-1}(t)\underline{\underline{B}}$. From these, the magnitudes of the burns required to transfer from a relative state $\underline{c}_0$ to the next desired one $\underline{c}_{des}$ (i.e., to achieve the variation $\Delta\underline{c}_{des}$) can be obtained by solving the system of linear equations shown in Eq. (64).

$$\underset{\underline{\eta}}{\text{maximize}}\, J_d = \underline{\eta}^T \Delta \underline{c}_{des} \quad \text{subject to} \quad \left\| \underline{\underline{B}}_c^T(t_i)\underline{\eta} \right\| \leq 1, \ \ t_j \in \left[t_0, t_f\right] \tag{63}$$

$$\left[\cdots\ \underline{\underline{B}}_c(t_i)\Delta\hat{v}(t_i)\ \cdots\right]\begin{bmatrix}\vdots\\ \left\|\Delta\underline{v}(t_i)\right\|\\ \vdots\end{bmatrix} = \Delta\underline{c}_{des} \tag{64}$$

As also observed in Ref. [30], usually the condition $\| \underline{\underline{B}}_c{}^T(t_i)\underline{\eta} \| = 1$ is not satisfied perfectly and requires considering a tolerance which can be selected as arbitrarily small. In general, larger tolerance values allow identifying more variegate transfer solutions at the cost of higher ΔVs.

2. Approach maneuver sequence

The approach sequence considered in the following is designed to gradually get the chaser closer to the target while also performing an inspection maneuver, leveraging the natural dynamics of the CR3BP to minimize the propellant consumption, and is articulated in three main phases. The first phase begins at $t_0 = 0$, with the chaser at 1 km of separation from the target object on the negative flight-path direction. After an initial waiting time of 0.005 orbits (i.e., about 1.27 h), the chaser performs a series of three transfers to gradually approach the target along the negative flight-path axis. Specifically, each transfer is computed to maneuver between bounded relative trajectories aligned along the flight-path direction, featuring predetermined minimum target-chaser distances of 500 m, 250 m, and 100 m, respectively. The three maneuvers are separated by waiting times of 0.005 orbits, which are introduced to replicate the necessity of an actual servicing mission to wait between two maneuvers to perform internal consistency checks before proceeding further. At the end of the last maneuver, the chaser further waits on its orbit for 0.005 orbits before resuming the operations. At this point, the second phase of the approach sequence begins, in which the chaser maneuvers onto a quasi-periodic relative trajectory that never violates a keep-out sphere of radius $r_{KOZ} = 25$ m centered in the target. This quasi-periodic motion is a desirable choice for target inspection as it allows the chaser to coast safely on this natural trajectory. After coasting for 5.05 orbits (i.e., about 53.35 days), in the last phase of the approach the chaser performs a maneuver towards a bounded relative trajectory that is once again aligned along the negative flight-path axis and never violates the minimum target-chaser separation of 25 m. This is considered a safe minimum distance for a bounded trajectory on which the chaser can wait for a final approach to occur and is coherent with the dimension of the keep-out sphere considered previously. An additional propagation of the motion is conducted for a full orbit after the end of the sequence to verify that the final condition is satisfied.

The sets of coefficients of the desired intermediate states constituting the approach sequence are summarized in Table 3 and are computed based on the methodology proposed in Section III.C, soliciting the center modes approximating the trivial motion or the actual center modes depending on the necessity. The initial state $\underline{c}_0$ is computed from the corresponding Cartesian representation according to Eq. (40). Notably, the possibility of evaluating how each ΔV affects the coefficients of modal decomposition using Eq. (62) allows computing all maneuvers in advance; Table 4 thus summarizes the segments of the approach sequence and the transfers that the chaser must perform, computed using the indicated sets of coefficients from Table 3, with an indication of the required ΔVs. The duration of each maneuver (that is, the time between two burns) is chosen to provide a feasible solution that achieves the required state.

Overall, the approach maneuver takes 7.701 orbits (i.e., about 81.36 days) to complete with a total ΔV of 2.104 cm/s. Observing Table 3, it is worth noting that states $\underline{c}_0$ and $\underline{c}_1$, $\underline{c}_2$, $\underline{c}_3$, and $\underline{c}_5$ expectedly share the same form, meaning that the motion corresponding to the set $\underline{c}_0$ is also a bounded one. In fact, a spacecraft located on the same orbit of the target satellite follows that orbit, resulting in a bounded motion that is almost aligned with the flight-path direction. A three-dimensional representation of the relative state of the chaser with respect to the target during the approach is shown in Fig. 10; however, the approach trajectory can be analyzed in greater detail by observing each phase separately.

Table 3 Summary of the desired intermediate states of the chaser during the approach maneuver.

State	Coefficients set	Description of corresponding state
$\underline{c}_0$	$[0, 0, 0, -1.283 \times 10^{-6}, 0, 0]$	Point at 1 km from target, on the negative flight-path direction.
$\underline{c}_1$	$[0, 0, 0, -6.415 \times 10^{-7}, 0, 0]$	Bounded motion along the negative flight-path direction, with a minimum target-chaser separation of 500 m.
$\underline{c}_2$	$[0, 0, 0, -3.208 \times 10^{-7}, 0, 0]$	Bounded motion along the negative flight-path direction, with a minimum target-chaser separation of 250 m.
$\underline{c}_3$	$[0, 0, 0, -1.283 \times 10^{-7}, 0, 0]$	Bounded motion along the negative flight-path direction, with a minimum target-chaser separation of 100 m.
$\underline{c}_4$	$[0, 0, -4.438 \times 10^{-7}, 0, 0, 0]$	Quasi-periodic motion around the target, with a keep-out sphere of radius 25 m centered in the target.
$\underline{c}_5$	$[0, 0, 0, -3.208 \times 10^{-8}, 0, 0]$	Bounded motion along the negative flight-path direction, with a minimum target-chaser separation of 25 m.

Table 4 Chaser approach strategy, with indication of the transfers, times of flight, and corresponding ΔVs.

Phase	Approach segment		Initial time, orbits	Final time, orbits	ΔV, cm/s
	ID	Description			
1	W1	Waiting	0	0.005	--
	T1	Transfer from $\underline{c}_0$ to $\underline{c}_1$	0.005	0.105	1.134
	W2	Waiting	0.105	0.110	--
	T2	Transfer from $\underline{c}_1$ to $\underline{c}_2$	0.110	0.210	0.587
	W3	Waiting	0.210	0.215	--
	T3	Transfer from $\underline{c}_2$ to $\underline{c}_3$	0.215	0.515	0.278
	W4	Waiting	0.515	0.520	--
2	T4	Transfer from $\underline{c}_3$ to $\underline{c}_4$	0.520	1.470	4.736×10^{-2}
	IS	Inspection	1.470	6.520	--
3	T5	Transfer from $\underline{c}_4$ to $\underline{c}_5$	6.520	6.701	5.746×10^{-2}
	FP	Final propagation	6.701	7.701	--

a) Full-scale view.

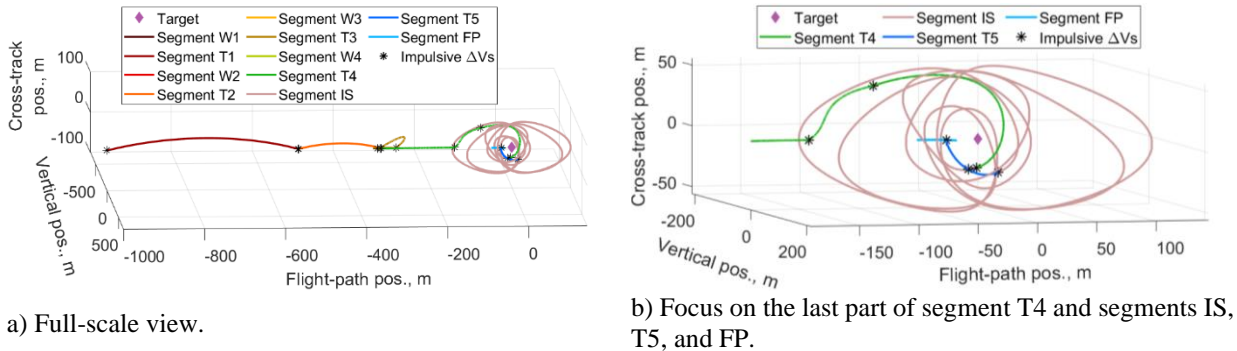b) Focus on the last part of segment T4 and segments IS, T5, and FP.

Fig. 10 Three-dimensional view of the relative motion of the chaser during the full approach sequence.

The first phase of the approach is illustrated in Fig. 11 in terms of both the temporal evolutions of the Cartesian state vector and the coefficients of modal decomposition. In this respect, Fig. 11.a shows that when the origin and target states of the transfer are on the flight-path axis, a cost-effective solution is that of an "hop" between the two points, involving both a vertical and a cross-track component. Notably, the last hop requires a longer time to be executed, as shorter times of execution may lead to unfeasible solutions that do not allow reaching the desired state. The first phase of the approach is represented in the ROE state space in Fig. 11.b, and Table 5 reports the values of the sets of coefficients that have been achieved at the end of each of the first three transfers. Compared to the target values $\underline{c}_1$, $\underline{c}_2$ and $\underline{c}_3$ in Table 3, the sets achieved at the end of transfers T1, T2 and T3 all feature large errors on the first, fifth, and last coefficients of the set. Specifically, on transfer T1 the coefficients of the stable and unstable modes

of the motion are almost equivalent in magnitude and opposite in sign, and they provide a drifting contribution towards the negative flight-path direction to the final natural motion. The situation changes for transfer T2, where the two modes contribute overall with a drift towards the positive flight-path direction, due to the sixth coefficient being the largest in magnitude; the same contribution can be observed for transfer T3, although it is related to the fact that the two coefficients are similar in magnitude and opposite in sign, with the first coefficient being positive and the last one being negative. During all three transfers, the fifth mode contributes with a drift term towards the negative flight-path direction. Overall, however, all the drifting contributions are negligible over the short waiting time that follows each maneuver. As a final remark, observing Fig. 11.b it is worth noting that the large values achieved by the fifth coefficient across the maneuvers are a direct consequence of the fact that the entries of eigenvector $\underline{v}_5$ are close to zero, thus requiring large values of the corresponding coefficient in order for this mode to affect the motion.

a) Cartesian components of relative motion.   b) Coefficients of modal decomposition.
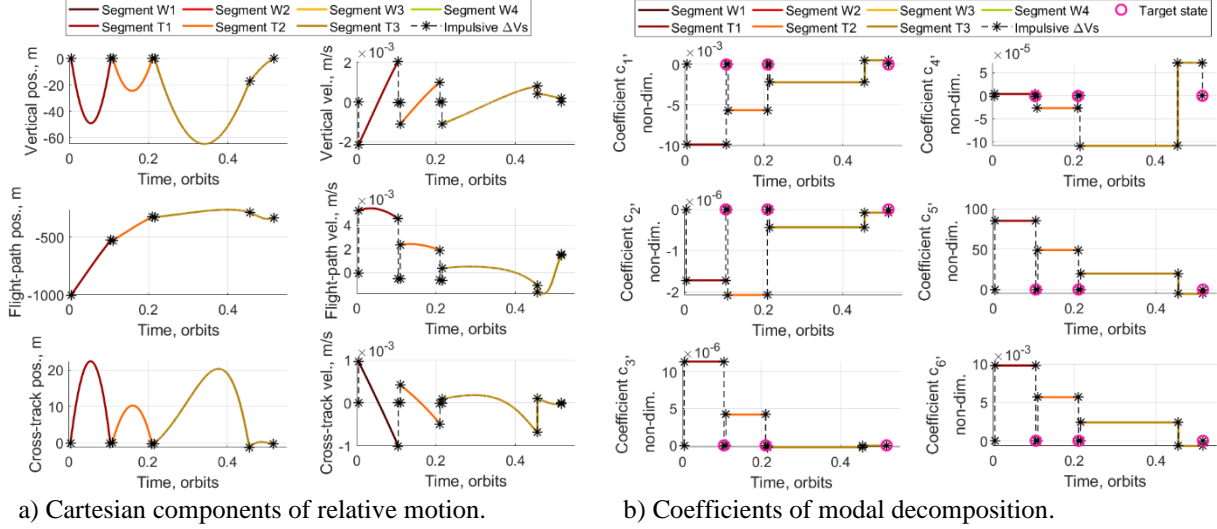
Fig. 11 Temporal evolution of the Cartesian state vector and the coefficients of modal decomposition during Phase 1 of the approach. Dashed black lines between asterisks represent discontinuities due to the application of a ΔV.

Table 5 Achieved target states $\hat{\underline{c}}_1$, $\hat{\underline{c}}_2$ and $\hat{\underline{c}}_3$ for the first phase of the approach.

Transfer segment	Achieved state
T1	$[-1.176 \times 10^{-8}, -5.515 \times 10^{-9}, -8.542 \times 10^{-9}, -6.421 \times 10^{-7}, -3.853 \times 10^{-5}, 1.274 \times 10^{-8}]$
T2	$[-8.915 \times 10^{-9}, 1.408 \times 10^{-9}, 5.221 \times 10^{-10}, -3.229 \times 10^{-7}, -8.928 \times 10^{-5}, -3.154 \times 10^{-8}]$
T3	$[5.121 \times 10^{-7}, -4.933 \times 10^{-9}, 5.889 \times 10^{-9}, -7.284 \times 10^{-8}, -4.876 \times 10^{-3}, -6.242 \times 10^{-7}]$

The second phase of the approach is illustrated in Fig. 12, showing that the transition from the oscillatory motion along the flight-path axis to the quasi-periodic motion of the center modes requires at least three impulses to occur. However, Fig. 12.a and Table 4 highlight that such impulses are small compared to those that have occurred in the first phase and amount to the orders of the tenths of mm/s. This is in line with the slow dynamics that naturally characterize the CR3BP, as evident by observing the magnitude of the velocity components achieved during the inspection motion. Therefore, for these maneuvers to take place and leverage the natural relative motion, propulsive units capable of providing ΔVs below mm/s-level are required. Table 6 contains the set of coefficients achieved at the end of transfer T4, showing that the largest error is achieved once again on the coefficients of the drifting modes and on the fifth coefficient of the drifting term of the trivial motion. Because the error on the coefficient of the unstable mode is negative and larger in magnitude than the one on the coefficient of the stable mode and the fifth coefficient is negative and four orders of magnitude larger than the other two, the three drifting contributions approximately balance each other over the considered time interval. As a result, the center of the quasi-periodic trajectory oscillates around the target, and the smallest target-chaser separation achieved during the motion amounts to 20.43 m.

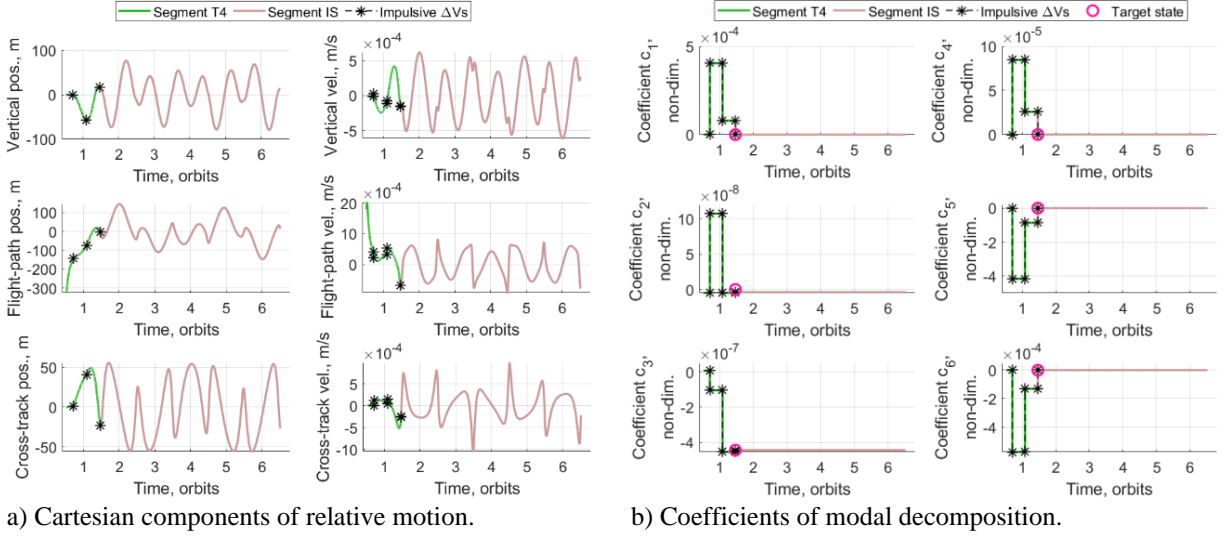a) Cartesian components of relative motion. b) Coefficients of modal decomposition.

Fig. 12 Temporal evolution of the Cartesian state vector and the coefficients of modal decomposition during Phase 2 of the approach. Dashed black lines between asterisks represent discontinuities due to the application of a ΔV.

Table 6 Achieved target state $\hat{\underline{c}}_4$ for the second phase of the approach.

Transfer segment	Achieved state
T4	$[2.496 \times 10^{-8}, -3.838 \times 10^{-9}, -4.435 \times 10^{-7}, 2.642 \times 10^{-9}, -2.990 \times 10^{-4}, -3.177 \times 10^{-8}]$

The third and last phase of the approach is illustrated in Fig. 13 and includes the final propagation of the motion after the last maneuver has occurred. The figure highlights that, expectedly, another three impulsive burns are required to maneuver from the quasi-periodic trajectory back to the flight-path axis, and the magnitude of the impulsive ΔVs is comparable to that observed in the previous case, as shown in Table 4.
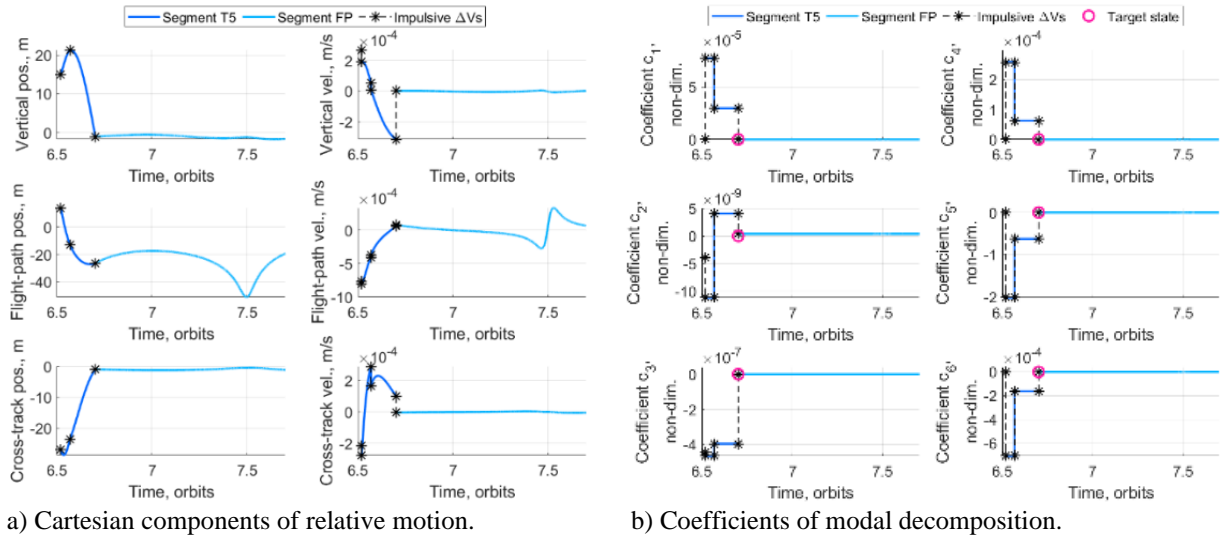

a) Cartesian components of relative motion. b) Coefficients of modal decomposition.

Fig. 13 Temporal evolution of the Cartesian state vector and the coefficients of modal decomposition during Phase 3 of the approach. Dashed black lines between asterisks represent discontinuities due to the application of a ΔV.

25

The final state achieved at the end of the transfer, reported in Table 7, once again shows that the three largest errors in achieving the final state occur on the first, fifth, and sixth coefficients of the set, and the same considerations of the previous case can be applied here as well. In fact, the positive sign of the coefficient of the unstable motion would imply a drift away from the target from a point in front of the latter; on the contrary, the negative sign of the sixth coefficient would result in a drift towards the target from a trailing point behind the latter. The motion that would result from the first and last coefficients only would therefore be a drifting motion away from the target and towards the positive flight path direction: the addition of the trivial mode, commanded by the fourth and fifth coefficient, results in a negligible drift of the chaser over the single orbit propagation occurring at the end of the approach, with the smallest target-chaser separation being 17.43 m.

Table 7 Achieved target state $\hat{\underline{c}}_5$ for the third phase of the approach.

Transfer segment	Achieved state
T5	$[3.574 \times 10^{-8}, 3.905 \times 10^{-10}, -4.140 \times 10^{-10}, -3.378 \times 10^{-8}, -3.051 \times 10^{-4}, -3.901 \times 10^{-8}]$

Overall, this test shows that it is possible to consider the coefficients of modal decomposition as geometrically insightful relative orbital elements for relative trajectory design. Moreover, the coefficients can be used in ROE-based path-planning and guidance algorithms to compute fuel-efficient maneuvers.

V. Conclusion

This paper presents a set of equations of relative motion in the context of the circular restricted three-body problem and an application of the method of fundamental modal solutions to these equations to gain geometrical insight in the motion that can be used for trajectory design and path planning. Specifically, the equations of relative motion are written in a velocity-based frame, centered in the target spacecraft and considering the instantaneous velocity direction as one of the fundamental directions of the right-handed orbiting frame. The equations feature an analytical formulation of the angular velocity of the velocity-based frame with respect to an inertial frame that allows immediate computation from the knowledge of the absolute state of the target spacecraft. The application of the method of the fundamental modal solutions then allows describing the fundamental components (i.e., the modes) of the motion separately as a function of the eigenvalues and eigenvectors of the monodromy matrix of the system of the linearized relative dynamics equations: by performing a weighted sum of the modes using a set of modal coefficients, any solution of the relative motion can be represented. Both the coefficients and the eigenvectors of the motion can be used to find characteristic geometric quantities of the motion, which help in designing the relative trajectories. The coefficients can therefore be used as geometrically insightful relative orbital elements. The application of the method of the fundamental modal solutions to the representation of the relative motion in the CR3BP provides a valuable instrument for the characterization of the motion and for mission design and planning. Mathematical relations are proposed to model important geometrical properties of the motion, relating them to the coefficients of the modal decomposition, and examples of application to the design of periodic, quasi-periodic, and drifting motion are provided. Finally, a way of employing the coefficients of modal decomposition as ROEs for the formulation of guidance and control solutions is proposed, showing the planning of an approach and inspection trajectory for a chaser spacecraft towards a target object on an L2 halo. The approach requires a total ΔV of 2.103 m/s for a total time of flight of about 81.36 days (corresponding to 7.701 orbits of the target object) but has the advantage of leveraging the natural dynamics of the CR3BP to coast on the approach trajectories and perform a passively safe inspection of the target.

The proposed methodologies are valid for their application in the CR3BP, but further improvements could be made first by investigating the applicability of the modal decomposition approach to more complex environments (for example, the elliptical restricted three-body problem, and models including the use of ephemerides). In addition, the method for the calculation of impulsive maneuvers considered in this work requires that the duration of the transfer be provided in advance. As the maneuvers cannot take place at any arbitrary point on the orbits of the target and chaser, further investigations may be conducted to improve the impulsive burn planning strategy by considering the most efficient points on the orbit to begin the transfer, based on the dynamics of the three-body problem. This would enable the possibility to explore the state-space of the coefficients to find more variegate solutions, thus providing the chaser with the ability to autonomously compute the transfers while also potentially enforcing trajectory and time-of-flight constraints.

Acknowledgments

References

[1] Luu, M., and Hastings, D. E., "Review of On-Orbit Servicing Considerations for Low-Earth Orbit Constellations," *ASCEND 2021*, AIAA Paper 2021-4207, AIAA, Las Vegas, NV, 2021.
doi: https://doi.org/doi:10.2514/6.2021-4207

[2] Opromolla, R., Grishko, D., Auburn, J., Bevilacqua, R., Buinhas, L., Cassady, J., Jäger, M., Jankovic, M., Rodriguez, J., Perino, M. A., and Bastida-Virgili, B., "Future In-Orbit Servicing Operations in the Space Traffic Management Context," *Acta Astronautica*, Vol. 220, Jul. 2024, pp. 469–477.
doi: https://doi.org/10.1016/j.actaastro.2024.05.007

[3] Duffy, L., and Adams, J., "Cislunar Systems Architectures Survey Paper,", *2022 IEEE International Systems Conference (SysCon)*, IEEE, Montreal, QC, Canada, 2022.
doi: https://doi.org/10.1109/SysCon53536.2022.9773886

[4] Johnson, K., "Fly Me to the Moon: Worldwide Cislunar and Lunar Missions," Center for Strategic and International Studies (CSIS), Washington, DC, USA, 2022.

[5] Sherman, W. A., Lightsey, E. G., and Whorton, M., "Envisioning Cislunar Formation Flight: A Survey and Analysis of Enabling Mission Topologies," *ASCEND 2023*, AIAA Paper 2023-4665, AIAA, Las Vegas, NV, 2023.
doi: https://doi.org/10.2514/6.2023-4665

[6] Guardabasso, P., Lizy-Destrez, S., and Ansart, M., "Lunar Orbital Debris Mitigation: Characterisation of the Environment and Identification of Disposal Strategies," *8th European Conference on Space Debris*, Vol. 8, ESA Space Debris Office, Darmstadt, Germany, 2021.

[7] Bhatiaa, S., Shahb, K., and Kamdarc, J., "Review of Strategies for Cis-Lunar Space Traffic Management," *73rd International Astronautical Congress (IAC)*, IAC-22-A6.IP, IAF, Paris, France, 2022.

[8] Corpino, S., and Stesina, F., "Inspection of the Cis-Lunar Station Using Multi-Purpose Autonomous Cubesats," *Acta Astronautica*, Vol. 175, Oct. 2020, pp. 591–605.
doi: https://doi.org/10.1016/j.actaastro.2020.05.053

[9] Bucchioni, G., and Innocenti, M., "Rendezvous in Cis-Lunar Space near Rectilinear Halo Orbit: Dynamics and Control Issues," *Aerospace*, Vol. 8, No. 3: 68, 2021.
doi: https://doi.org/10.3390/aerospace8030068

[10] Ceresoli, M., Zanotti, G., and Lavagna, M., "Bearing-Only Navigation for Proximity Operations on Cis-Lunar Non-Keplerian Orbits," 72nd International Astronautical Congress (IAC), IAC–21–C1.1.7, IAF, Dubai, United Arab Emirates, 2021.

[11] Segerman, A. M., Zedd, M. F., and Bauer, F. H., "Preliminary Planar Formation-Flight Dynamics near Sun-Earth L2 Point," *2003 AAS/AIAA Space Flight Mechanics Meeting*, AAS Paper 03-133, AAS/AIAA, Ponce, Puerto Rico, 2003.

[12] Luquette, R., and Sanner, R., "Linear State-Space Representation of the Dynamics of Relative Motion, Based on Restricted Three Body Dynamics," *AIAA Guidance, Navigation, and Control Conference and Exhibit*, AIAA Paper 2004-4783, AIAA, Providence, RI, 2004.
doi: https://doi.org/10.2514/6.2004-4783

[13] Colagrossi, A., Pesce, V., Bucci, L., Colombi, F., and Lavagna, M., "Guidance, Navigation and Control for 6DOF Rendezvous in Cislunar Multi-Body Environment," *Aerospace Science and Technology*, Vol. 114, Jul. 2021, 106751.
doi: https://doi.org/10.1016/j.ast.2021.106751

[14] Colombi, F., Colagrossi, A., and Lavagna, M., "Characterisation of 6DOF Natural and Controlled Relative Dynamics in Cislunar Space," *Acta Astronautica*, Vol. 196, Jul. 2022, pp. 369–379.
doi: https://doi.org/10.1016/j.actaastro.2021.01.017

[15] Franzini, G., and Innocenti, M., "Relative Motion Dynamics in the Restricted Three-Body Problem," *Journal of Spacecraft and Rockets*, Vol. 56, No. 5, 2019, pp. 1322–1337.
doi: https://doi.org/10.2514/1.A34390

[16] Elliott, I., and Bosanac, N., "Geometric Relative Orbital Element Set for Motion Near a Periodic Orbit with Oscillatory Modes," *2020 AAS/AIAA Astrodynamics Specialist Virtual Conference*, AAS Paper 20-620, AAS/AIAA, South Lake Tahoe, CA, 2020.

[17] Zuehlke, D., Sizemore, A., and Henderson, T., "Periodic Relative Natural Motion in the Circular Restricted Three-Body Problem," *Proceedings of the 33rd AAS/AIAA Space Flight Mechanics Meeting*, AAS/AIAA, Austin, Texas, 2023, pp. 23–112.

[18] Zuehlke, D., Tiwari, M., Jebari, K., and Kidambi, K. B., "Rendezvous and Proximity Operations in Cislunar Space Using Linearized Dynamics for Estimation," *Aerospace*, Vol. 10, No. 8: 684, 2023.
doi: https://doi.org/10.3390/aerospace10080674

[19] Mand, K., Woffinden, D., Spanos, P., and Zanetti, R., "Rendezvous and Proximity Operations at the Earth-Moon L2 Lagrange Point: Navigation Analysis for Preliminary Trajectory Design," *Advances in the Astronautical Sciences*, Vol. 152, AAS Paper 14-376, 2014, pp. 2425–2444.

[20] Bucci, L., Colagrossi, A., and Lavagna, M., "Rendezvous in Lunar Near Rectilinear Halo Orbits," *Advances in Astronautics Science and Technology*, Vol. 1, Sep. 2018, pp. 39–43.
doi: https://doi.org/10.1007/s42423-018-0012-6

[21] Brown, B. M., Eastham, M. S. P., and Schmidt, K. M., "Floquet Theory," *Periodic Differential Operators*, Springer Basel, Basel, 2013, pp. 1–29.
doi: https://doi.org/10.1007/978-3-0348-0528-5_1

[22] Sherrill, R. E., Sinclair, A. J., Sinha, S. C., and Lovell, T. A., "Time-Varying Transformations for Hill–Clohessy–Wiltshire Solutions in Elliptic Orbits," *Celestial Mechanics and Dynamical Astronomy*, Vol. 119, May 2014, pp. 55–73.
doi: https://doi.org/10.1007/s10569-014-9543-x

[23] Sherrill, R. E., Sinclair, A. J., Sinha, S. C., and Lovell, T. A., "Lyapunov-Floquet Control of Satellite Relative Motion in Elliptic Orbits," *IEEE Transactions on Aerospace and Electronic Systems*, Vol. 51, No. 4, 2015, pp. 2800–2810.
doi: https://doi.org/10.1109/TAES.2015.140281

[24] Ogundele, A. D., Agboola, O. A., and Sinha, S. C., "Application of Lyapunov–Floquet Transformation to the Nonlinear Spacecraft Relative Motion with Periodic-Coefficients," *Acta Astronautica*, Vol. 187, Oct. 2021, pp. 24–35.
doi: https://doi.org/10.1016/j.actaastro.2021.06.024

[25] Burnett, E. R., and Schaub, H., "Modal Decomposition of Spacecraft Relative Motion in Quasi-Periodic Orbits," *2020 AAS/AIAA Astrodynamics Specialist Virtual Conference*, AAS Paper 20-506, AAS/AIAA, South Lake Tahoe, CA, 2020.

[26] Burnett, E. R., and Schaub, H., "Geometric Perspectives on Fundamental Solutions in the Linearized Satellite Relative Motion Problem," *Acta Astronautica*, Vol. 190, Jan. 2022, pp. 48–61.
doi: https://doi.org/10.1016/j.actaastro.2021.09.028

[27] Burnett, E. R., and Schaub, H., "Spacecraft Relative Motion Dynamics and Control Using Fundamental Modal Solution Constants," *Journal of Guidance, Control, and Dynamics*, Vol. 45, No. 10, 2022, pp. 1786–1799.
doi: https://doi.org/10.2514/1.G006603

[28] Bai, X., Huang, M., Xu, M., and Liu, J., "Reconfiguration Optimization of Relative Motion Between Elliptical Orbits Using Lyapunov-Floquet Transformation," *IEEE Transactions on Aerospace and Electronic Systems*, Vol. 59, No. 2, 2022, pp. 923–936.
doi: https://doi.org/10.1109/TAES.2022.3193089

[29] Albert, S. W., and Schaub, H., "Relative Motion in the Velocity Frame for Atmospheric Entry Trajectories," *Journal of Spacecraft and Rockets*, Vol. 60, No. 5, 2023, pp. 1614–1624.
doi: https://doi.org/10.2514/1.A35753

[30] Guffanti, T., and D'Amico, S., "Integration Constants as State Variables for Optimal Path Planning," *2018 European Control Conference (ECC)*, IEEE, Limassol, Cyprus, 2018, pp. 3197–3202.
doi: https://doi.org/10.23919/ECC.2018.8550448